https://doi.org/10.5194/egusphere-2026-6260
Preprint. Discussion started: 19 November 2026
© Author(s) 2026. CC BY 4.0 License.

Synoptic-scale meteorology modulates aerosol and fog characteristics in coastal Namibia

Huihui Wu[1], Chenjie Yu[1], Vincent Michoud[1], Hendrik Andersen[2,3], Aneska Richter[4], Henno Havenga[4], Brigitte Language[4], Daniel Tetteh Quaye[5], Khanneh Wadinga Fomba[5], Laurent Poulain[5], Uwe Käfer[5], Muguette Allegre[1], Cécile Gaimoz[1,a], Mathieu Cazaunau[1], Maxime Feingesicht[1], Hupenyu Allan Mupambwa[6], Stuart John Piketh[4], and Paola Formenti[1]

[1] Université Paris Cité and Univ Paris Est Créteil, CNRS, LISA, F-75013 Paris, France
[2] Karlsruhe Institute of Technology (KIT), Institute of Meteorology and Climate Research Atmospheric Trace Gases and Remote Sensing, Karlsruhe, Germany
[3] Karlsruhe Institute of Technology (KIT), Institute of Photogrammetry and Remote Sensing, Karlsruhe, Germany
[4] School of Geo- and Spatial Science, North-West University, Potchefstroom, South Africa
[5] Leibniz Institute for Tropospheric Research (TROPOS), Leipzig, Germany
[6] Sam Nujoma Marine and Coastal Resources Research Centre, University of Namibia, Sam Nujoma Campus, Private Bag 462, Henties Bay 13005, Namibia
[a] now at: CNRS INSU Division Technique, Gif-Sur-Yvette, France

Correspondence to: Chenjie Yu (chenjie.yu@lisa.ipsl.fr) and Paola Formenti (paola.formenti@lisa.ipsl.fr)

Abstract. Fog is an important water source for the hyper-arid Namib ecosystem, yet the coupled effects of meteorology and aerosols on fog formation and microphysics remain poorly constrained. Here, we present comprehensive observations from an intensive field campaign conducted in May 2024 at Henties Bay, a Namibian coastal site. Three representative meteorological regimes were identified. Dominant continental outflow with intermittent sea-breeze influence produced broad aerosol size distributions and the lowest hygroscopicity due to externally mixed continental and marine aerosols. The associated warm, dry conditions were unfavorable for fog formation. Southeasterly coastal flow along the Benguela region was characterized by dominant Aitken-mode particles and moderate hygroscopicity, whereas westerly oceanic flow transported cloud-processed marine aerosols with low particle loadings and the highest accumulation-mode hygroscopicity. Seven fog events were observed. Fog formed locally in a shallow moist boundary layer that was capped by warm and dry subsiding continental easterlies, which was likely influenced by both radiative and advective cooling. These events exhibited generally higher fog supersaturation and greater variability in microphysical properties than fog events resulting from the lowering of advected marine stratus under westerly oceanic flow. Peak droplet number concentrations were positively correlated with pre-fog aerosol number concentrations, indicating that aerosol abundance modulated droplet activation. Overall, synoptic-scale meteorology primarily controlled fog occurrence, formation pathways, and supersaturation, while aerosols further modulated fog microphysics. These observations provide quantitative constraints on aerosol-fog parameterizations under contrasting coastal meteorological regimes and highlight the necessity to consider different fog-formation pathways when assessing aerosol-fog interactions in Namibia.

https://doi.org/10.5194/egusphere-2026-6260
Preprint. Discussion started: 19 November 2026
© Author(s) 2026. CC BY 4.0 License.

1 Introduction

Southern Africa is widely recognized as a climate change hotspot, where projected warming is expected to amplify extremes in a naturally warm, dry, and water-stressed region (Engelbrecht et al., 2024). Namibia is particularly vulnerable because much of the country is arid to hyper-arid, and climate projections indicate continued aridification (Rohde et al., 2019). In the Namibian coastal system, fog represents a key climatic component, which can provide a more reliable water source than episodic rainfall and sustain local biological communities (Shanyengana et al., 2002; Mitchell et al., 2020). In addition, fog can transport nutrients and pollutants, thereby influencing regional biogeochemical cycling (Weathers et al., 2020).

Several mechanisms have been proposed to explain fog formation along the Namibian coast and in the central Namib Desert. Near the coast, advection fog can form when moist marine air is advected over the cold Benguela ocean surface, which is restricted to a narrow coastal zone (Olivier and Stockton, 1989; Seely and Henschel, 1998). Further inland, fog occurrence is frequently linked to the advection of marine low stratus clouds and their intersection with elevated terrain, which can extend more than 100 km inland (Seely and Henschel, 1998; Spirig et al., 2019). Recent years have seen coordinated efforts to constrain the occurrence, life cycle, and spatial distribution of Namib fog. The distributed FogNet stations have provided long-term observations of local meteorology, including fog occurrence, which have also been complemented by fog water stable isotope measurements (Kaspar et al., 2015; Li et al., 2026). Building on this network, the NaFoLiCA (Namib Fog Life Cycle Analysis) project developed complementary approaches that integrated ground and satellite observations to understand regional fog patterns (Andersen and Cermak, 2018; Spirig et al., 2019). Multi-year analyses indicate that synoptic-scale circulation controls Namib fog occurrence, and advected marine fog and low stratus dominate the regional fog, where stratus base altitude defines fog occurrence (Andersen et al., 2019, 2020; Hipler et al., 2026; Malik et al. 2026). Nevertheless, stable-isotope measurements of fog samples across inland FogNet stations have been interpreted to point to the occurrence of locally formed fog, which may account for a substantial fraction of observed fog events (Kaseke et al., 2017, 2018). However, the mechanisms underlying locally formed fog remain incompletely understood, particularly the relative roles of radiative cooling and advective processes. Although previous studies have improved the understanding of Namib fog occurrence and its dynamical controls, fog microphysics associated with different formation pathways has also not been systematically assessed, while it can influence fog persistence and the deposition of water and nutrients (Nelli et al., 2024).

In addition, the role of aerosols in fog formation and microphysics remains poorly characterized. Aerosols can act as cloud condensation nuclei (CCN) and provide surfaces on which water vapor condenses to form fog droplets (Petters and Kreidenweis, 2007). The number of activated droplets and their size distributions can be modulated by aerosol CCN ability, which depends on aerosol physicochemical properties including size distribution and composition (Petters and Kreidenweis, 2007). Previous observations have demonstrated generally positive relationships between fog droplet number concentrations and pre-fog aerosol concentrations (Duplessis et al., 2021; Liu et al., 2025). Greater CCN availability can produce more numerous but smaller droplets, enhancing light extinction and fog lifetime (Mazoyer et al., 2019; Yan et al., 2021). However, this response is nonlinear because competition for the limited water vapor can suppress supersaturation and restrict further

https://doi.org/10.5194/egusphere-2026-6260
Preprint. Discussion started: 19 November 2026
© Author(s) 2026. CC BY 4.0 License.

aerosol activation, emphasizing the combined role of aerosol and meteorological conditions in governing fog formation and development (Mazoyer et al., 2019). Efforts have consequently been made to represent the role of aerosols in simulating the fog life cycle (Boutle et al., 2018; Poku et al., 2021; Weston et al., 2022; Ghosh et al., 2025). In these models, the number of activated droplets is calculated from aerosol size distributions and hygroscopicity or composition, together with meteorological conditions, using Köhler theory or activation parameterizations.

Long-term ground-based aerosol observations have been conducted at Henties Bay and Gobabeb Observatory, complemented by the comprehensive AEROCLO-sA (AErosols, RadiatiOn and CLOuds in southern Africa) campaign at Henties Bay during August-September 2017 (Formenti et al., 2018, 2019, 2025; 2026; Klopper et al., 2020). These studies demonstrate complex aerosol sources in this region, including sea salt, mineral dust, and marine biological emissions, as well as episodic biomass-burning and anthropogenic emissions. Consequently, aerosol abundance and composition are strongly modulated by seasonal circulation and land-sea-breeze transport (Formenti et al., 2018; Klopper et al., 2020). Such source-dependent variability complicates the representation of aerosol effects on fog formation and microphysics, however, corresponding variations in aerosol properties remain insufficiently characterized, particularly aerosol CCN ability.

Moreover, comprehensive observations simultaneously resolving aerosol properties and fog microphysics remain scarce in Namibia, e.g., only two fog events during AEROCLO-sA. Weston et al. (2022) evaluated aerosol activation and fog microphysics for the two fog events using the aerosol-aware microphysics scheme implemented in the Weather Research and Forecasting (WRF) model. Observationally constrained CCN concentrations alone were insufficient to reproduce the observed fog microphysics, partly because the activation scheme was controlled by updraft-driven cooling locally, whereas the observed fog events were more associated with the advection and cloud-base-lowering of marine stratus. Aerosol effects on fog cannot be assessed independently of fog-formation types, because they differ in droplet activation and in the cooling and vertical motion that control supersaturation (Poku et al., 2021; Pope and Igel, 2025). Further cases combining simultaneous measurements of aerosol properties and fog microphysics under different fog-formation conditions are therefore required.

In this study, we address the gaps discussed above, using observations during the first intensive campaign of the AEROFOG (AEROsols and FOG in southern Africa: processes and impact on biogeochemistry) project. The campaign provided coordinated and comprehensive observations of gases, aerosols, fog, and meteorology at Henties Bay in May 2024, a site located on the Namibia coastline. This region provides a unique natural laboratory for investigating coastal fog and aerosol-fog interactions under different conditions, as it lies at the interface between the cold Benguela upwelling system, marine boundary layer, and African continental outflow. Specifically, this study aims to (1) characterize source-dependent aerosol physicochemical properties and CCN activity; (2) investigate the microphysical properties of locally formed fog and advection-driven fog from lowering marine stratus separately; and (3) understand the roles of meteorological conditions and aerosol properties in modulating fog occurrence, formation pathways, and microphysics.

https://doi.org/10.5194/egusphere-2026-6260
Preprint. Discussion started: 19 November 2026
© Author(s) 2026. CC BY 4.0 License.

2 Methods

2.1 Measurement site and sampling period

A ground-based field campaign took place from 12 May to 1 June 2024 at the Henties Bay Research Centre of the University of Namibia (22°09′S, 14°26′E; 20 m above mean sea level). The campaign was the first intensive observation phase of the AEROFOG project. Henties Bay is located on the Namibia western coast, where fog and low stratus clouds occur frequently from March to May (Dorman et al, 2020). The site is well suited for examining how different meteorological regimes and aerosol sources influence fog formation and microphysics. Aerosol and gas-phase measurements were conducted using the ground-based mobile laboratory Portable Gas and Aerosol Sampling Units (PEGASUS), which was equipped with a comprehensive suite of instruments (Formenti et al., 2019). Additional measurement systems included fog-droplet probes, fog-water collectors and radiosonde. A separate meteorological station provided observations of surface temperature, pressure, wind direction and speed, and relative humidity (RH). The key aerosol and fog instruments used in this study are described in the following section.

2.2 Instrumentation

2.2.1 Aerosol measurements

The size-resolved CCN activity of aerosol particles was characterized following the approach described by Pöhlker et al. (2016). After drying, polydisperse aerosol particles were neutralized using a soft Xray radioactive source and then introduced into a differential mobility analyzer (DMA, TSI 3081). The DMA selected monodisperse particles with a mobility diameter between 10 and 500 nm. The size-selected aerosol flow was subsequently split between a condensation particle counter (CPC, TSI 3775) and a Cloud Condensation Nucleus counter (CCNc, model CCN-100, DMT). The DMA sheath flow was set to 5 L min^{-1}, and the CPC sample flow was set to 0.3 L min^{-1}. The inlet flow rate of the CCNc was set to 0.5 L min^{-1}, with a sheath-to-aerosol flow ratio of 10. At each selected particle dry size, the number concentrations of condensation nuclei (CN) were measured by the CPC, and CCN concentrations (N_{CCN}) were measured by the CCNc (Fig. S1a in the supplement). The CCN activation fraction (N_{CCN}/CN) was then obtained as a function of particle dry size. For a given water supersaturation (*SS*), the activation diameter (D_c) was determined as the dry diameter at which 50 % of the particles were activated (N_{CCN}/CN = 0.5) (Fig. S1b in the supplement). The *SS* for CCNc was set to 0.1%, 0.2%, 0.3%, 0.4%, and 0.5%, with time interval of 10 min for each *SS* during the experiment.

The DMA-CPC system described above is the set-up of a scanning mobility particle sizer (SMPS), which provided aerosol number size distributions in the mobility diameter range of 10–500 nm at a time resolution of 3 min. Mobility diameter measured by the DMA can be converted into geometrical diameter by dividing for the dry dynamic shape factor, which was set to 1 in our study assuming spherical particles (DeCarlo et al., 2004). In addition, an optical particle counter (OPC, GRIMM 1.109 mode) was employed to measure aerosol number size distributions in the size range of 0.25–32 µm at a time resolution of 1 min. The GRIMM OPC classifies particles based on their optical diameter defined by the light scattering signal intensity

https://doi.org/10.5194/egusphere-2026-6260
Preprint. Discussion started: 19 November 2026
© Author(s) 2026. CC BY 4.0 License.

derived from interaction with a monochromatic light source (Heim et al., 2008). The total number concentration in submicron range (N_a) was calculated by summing up number concentrations from SMPS total size bins and GRIMM size bins from 0.5 to 1 µm.

Non-refractory aerosol chemical composition was measured using a Time-of-Flight Aerosol Chemical Speciation Monitor with eXtended Resolution (ToF-ACSM-X, Aerodyne Research Inc., USA). The instrument provides real-time measurements of organic aerosol (OA), sulfate, nitrate, ammonium, and chloride, over a vacuum aerodynamic diameter range of ~70–800 nm. Compared with conventional unit-mass-resolution ACSM measurements, it enables high-resolution ion fitting and improved elemental analysis (Nault et al., 2025). Ambient aerosol particles were sampled through an aerodynamic lens and focused into a narrow particle beam. Particles were flash vaporized on a standard vaporizer at ~600 °C and subsequently ionized by 70 eV electron impact. The generated ions were analyzed by the time-of-flight mass spectrometer. Data was acquired at 1 Hz and averaged to a time resolution of 10 min. The raw data were processed using Tofware 4.1.1 within Igor Pro. High-resolution peak fitting was applied to derive mass concentrations of OA, nitrate, sulfate, ammonium, and chloride. The ionization efficiency was calibrated using size-selected ammonium nitrate particles. The oxygen-to-carbon ratio (O:C) was calculated using the elemental analysis described by Canagaratna et al. (2015).

2.2.2 Fog droplet measurements

A Forward Scattering Spectrometer Probe (FSSP) was used to measure fog droplet size distributions in the size range of 3 to 50 µm. The instrument sizes individual droplets based on the intensity of forward-scattered laser light and records particle counts in discrete diameter bins (Baumgardner, 1983; Doulgeris et al., 2020). Bin-resolved droplet number concentrations were obtained by normalizing raw counts by the sampling volume, which was calculated from the true air speed, the effective probe sampling area, and the sampling interval. The effective sampling area was defined as the beam width multiplied by the depth of field, with a correction based on the beam acceptance ratio. From the bin-resolved concentrations, the total droplet number concentration (N_d) was derived by integrating the droplet size distribution based on the Eq. (1).

$$N_d = \int n(r)\, dr \approx \sum_1^m n(r_i) \quad (1)$$

The LWC was derived based on the Eq. (2), assuming spherical water droplets and a liquid water density (ρ_{water}) of 1 g cm^{-3}.

$$LWC = \frac{4\pi}{3} \rho_{water} \int r^3\, n(r)\, dr \approx \frac{4\pi}{3} \rho_{water} \sum_1^m r_i^3\, n(r_i) \quad (2)$$

The R_e was derived based on the Eq. (3).

$$R_e = \frac{\int r^3\, n(r)\, dr}{\int r^2\, n(r)\, dr} \approx \frac{\sum_1^m r_i^3\, n(r_i)}{\sum_1^m r_i^2\, n(r_i)} \quad (3)$$

where $n(r_i)$ is the droplet number concentration in each size bin, and r_i is the middle radius for each size bin. The uncertainties in these microphysical parameters were estimated using a Monte Carlo error propagation approach. The uncertainty in droplet counts for each size bin was represented using Poisson counting statistics. Additional uncertainties, e.g., true air speed (5%), beam width (5%), and droplet sizing (10%), were included by perturbing these quantities according to prescribed relative uncertainties (Baumgardner, 1983; Dye and Baumgardner, 1984).

https://doi.org/10.5194/egusphere-2026-6260
Preprint. Discussion started: 19 November 2026
© Author(s) 2026. CC BY 4.0 License.

2.3 Estimation of hygroscopicity parameter

2.3.1 CCNc-based hygroscopicity parameter (κ_{CCN})

Figure S1 in the supplement provides typical examples of the size-resolved CCN activation fraction (N_{CCN}/CN) during the experiment, and this curve can be fitted in sigmoid function to derive D_c. By applying the CCNc-measured D_c into κ-Köhler relationship (Eq. (4)) (Petters and Kreidenweis, 2007), the κ_{CCN} can be obtained by matching the critical supersaturation, which is the maximum supersaturation on the Köhler curve, as configured in the CCNc.

$$\kappa = \frac{4A^3}{27D_P^3 ln^2 S_{crit}} \quad (4)$$

where D_p is the dry particle diameter, S_{crit} is the supersaturation set by the CCNc, and A is the Kelvin term calculated from Eq. (5):

$$A = \frac{4\sigma M_w}{RT\rho_w} \quad (5)$$

where σ is the surface tension (σ = 0.072 J m^{-2}), R is the universal gas constant, M_w is the molecular weight of water, and ρ_w is the density of water. In the κ-Köhler model, higher values of κ indicate a more hygroscopic particle that is more efficient at taking up water and that can activate as CCN at lower *SS*.

2.3.2 Chemical hygroscopicity parameter (κ_{chem})

The κ_{chem} of a mixed particle was calculated using volume-weighted contributions of different species and their corresponding κ values, applying the Zdanovskii-Stokes-Robinson (ZSR) mixing rule (Petters and Kreidenweis, 2007):

$$\kappa_{chem} = \sum_i \varepsilon_i \kappa_i \quad (6)$$

where ε_i and κ_i represents the volume fraction and κ value of chemical component i, respectively. The ToF-ACSM-X provides mass concentrations of OA, nitrate, sulfate, ammonium, and chloride fragments. A simplified ion-pairing scheme was applied to infer the mass concentrations of complete inorganic components, following the approaches of Gysel et al. (2007) and Mandariya et al. (2024). The scheme includes sulfuric acid, ammonium sulfate, ammonium bisulfate, ammonium nitrate, and ammonium chloride. The ToF-ACSM-X is not expected to vaporize and quantify refractory sea-salt components. However, sodium-chloride-related ion signals (e.g. Na^+ and $NaCl^+$) were detected by the ToF-ACSM-X at this coastal site, indicating the influence of sea-salt-containing particles. Similar partial detection of sea-salt-related fragments by aerosol mass spectrometry has also been reported previously in marine environments (Schmale et al., 2013; Huang et al., 2018). Chloride that could not be paired with ammonium in the ion-pairing procedure was potentially associated with sea salt. Although sea-salt mass concentrations could be estimated from the $NaCl^+$ ion using an appropriate scaling factor (Ovadnevaite et al., 2012; Huang et al., 2018), sea-salt calibration was not performed for the ToF-ACSM-X used in this study. Sea-salt mass was therefore not quantified and excluded from the κ_{chem} calculation. Consequently, κ_{chem} may be underestimated when sea salt contributed to

https://doi.org/10.5194/egusphere-2026-6260
Preprint. Discussion started: 19 November 2026
© Author(s) 2026. CC BY 4.0 License.

the sampled aerosol. The mass concentrations of all inferred chemical components were converted to volume concentrations using assumed densities, and the resulting volume fractions were then used in Eq. (6). Values of κ and densities used for chemical components are summarized in Table S1 in the supplement.

2.4 Estimation of the *SS* in fog

Fog supersaturation is a key thermodynamic parameter governing aerosol activation and subsequent fog microphysical development, but it is difficult to measure directly under ambient conditions. Aerosol particles can activate into fog droplets when the ambient supersaturation exceeds its critical supersaturation. Equivalently, at a given supersaturation, particles larger than the corresponding critical dry diameter are expected to activate. Assuming that N_d in the fog represents the number concentration of activated CCN (N_{CCN}), the fog supersaturation (SS_{CCN}) was inferred by identifying the supersaturation at which N_{CCN} equaled N_d (Fig. S2 in the supplement). This value was obtained by piecewise linear interpolation of the *SS*-resolved N_{CCN} measurements (Liu et al., 2025). The selected periods of N_{CCN} measurements for the SS_{CCN} retrieval are described in Sect. 3.3.2. Since the lowest *SS* set point of CCNc was 0.1 %, *SS* values less than 0.1 % were estimated from extrapolation of the linear extension line (dashed black line in Fig. S2 in the supplement).

2.5 Backward dispersion simulations

To investigate the origin and transport history of airmasses at Henties Bay, backward dispersion simulations were performed using the UK Met Office's Numerical Atmospheric Modeling Environment (NAME) (Jones et al., 2007). NAME was selected for this study due to its ability to utilize high-resolution meteorological data, with a grid resolution of approximately 10 km × 10 km. It can simulate dispersion over a wide range of spatial scales, from a few kilometers to global distances. A specified number of hypothetical tracer particles were released from Henties Bay. The trajectories of released tracer particles were tracked backward for 2 days, based on three-dimensional gridded meteorological fields from the UK Met Office's Unified Model (MetUM) (Brown et al., 2012). These meteorological fields were updated every three hours, with a high horizontal resolution of 0.14° longitude by 0.1° latitude and 59 vertical levels extending up to ~ 29 km in altitude. In this study, the integrated horizontal footprints within the boundary layer were output for each simulation, representing the cumulative air parcels passing through each grid over the past two days. The footprints are expressed in units of mass concentration (g m^{-3}), based on the predetermined quantity of released air parcels.

2.6 Satellite and reanalysis data

Fog and low-cloud (FLC) occurrence over the study region was characterized using the Spinning Enhanced Visible and Infrared Imager (SEVIRI) onboard Meteosat Second Generation satellites. Over land, FLC occurrence was retrieved following the algorithm of Andersen and Cermak (2018). This approach identifies fog and low clouds from SEVIRI thermal infrared observations, using spectral and contextual tests. As this approach relies on a structural similarity comparison with cloud-free land-surface composites, and requires stable spatial structures in the thermal infrared, it is only applicable over land. Over the

https://doi.org/10.5194/egusphere-2026-6260
Preprint. Discussion started: 19 November 2026
© Author(s) 2026. CC BY 4.0 License.

ocean, low-level cloud occurrence was derived from the instantaneous CLAAS-3 SEVIRI cloud-top products, which provide cloud-mask and cloud-top properties (Benas et al., 2023). Cloudy pixels with cloud-top temperature higher than 280 K were classified as warm low-level clouds. Daily FLC occurrence duration over the study region was then summarized between 00:00 and 09:00 UTC, corresponding to the main nocturnal-to-morning fog period at Henties Bay. A value of 9 hours therefore represents continuous FLC presence throughout the 00:00 and 09:00 UTC period. It is noted that falsely detected low clouds in a narrow coast-parallel band are visible in the CLAAS-3 data, particularly May 18–20. Satellite maps are intended to provide a qualitative perspective on fog and low cloud distribution in the region.

Large-scale meteorological conditions were characterized using the fifth-generation atmospheric reanalysis produced by the European Centre for Medium-Range Weather Forecasts (ECMWF), ERA5 (Hersbach et al., 2020). ERA5 provides global, hourly meteorological fields by assimilating multiple observational datasets (station data, radiosondes, and satellites) into a numerical model. It has a horizontal resolution of 0.25° and a vertical resolution of 25 – 50 hPa. The analyzed variables in this study included air temperature, specific humidity (Q), RH, and wind components (U, V, W).

3 Results and discussion

3.1 Airmass history and case classification

Backward dispersion fields can represent the horizontal footprints of source air parcels transported over the preceding two days before reaching the Henties Bay site. Figure 1 shows period-integrated backward dispersion fields, with each period exhibiting broadly consistent footprint patterns. From 16 to 23 May and on 27 May, the integrated backward dispersion field (Fig. 1a) indicates that the majority of surface air masses originated from the northeastern continental region, with additional contributions from the southeastern coastal region. During this period, strong continental winds generally prevailed from midnight to midday, followed by a transition to southeasterly winds in the afternoon driven by the development of local sea breeze (Fig. S3a in the supplement). Consistently, surface observations showed a pronounced diurnal cycle in temperature and RH. Easterly continental flow was associated with high temperatures, reaching up to 40 °C around midday, and low RH, whereas the afternoon sea-breeze was associated with lower temperatures and higher RH (Fig. S3b in the supplement). From 24 to 26 May, the surface air masses were still influenced by easterly continental winds, but predominately from the southeastern region, with source air parcels transporting along the west coast of Africa (Fig. 1b). From 28 to 30 May, the surface air masses originated predominantly from the western oceanic region (Fig. 1c). Compared with the first period, these latter two periods were characterized by more stable surface meteorological conditions, with persistently low surface temperatures and high RH (Fig. S3b in the supplement). In addition, at the beginning of the campaign (12 to 15 May), the site was in a transitional regime, shifting from dominant coastal flow toward stronger easterly continental outflow.

Figure 2a shows campaign-average mass concentrations of ocean surface chlorophyll-a, which was derived from the Copernicus Climate Change Service Ocean Color product (Copernicus Climate Change Service, 2019). Chlorophyll-a is used here as a proxy for phytoplankton biomass and marine biological activity (Rinaldi et al., 2013). Elevated chlorophyll-a

https://doi.org/10.5194/egusphere-2026-6260
Preprint. Discussion started: 19 November 2026
© Author(s) 2026. CC BY 4.0 License.

concentrations were observed in the Benguela coastal upwelling region, which could be associated with enhanced marine biogenic emissions. Figures 2b and 2c show the average emission fluxes of anthropogenic NOx and biogenic isoprene for May 2024, respectively, which were retrieved from the published emission inventories (Copernicus Atmosphere Monitoring Service, 2020). They provide proxies for anthropogenic and terrestrial biogenic emission strengths. From 16 to 23 May and on 27 May, Henties Bay was influenced by anthropogenic and potentially terrestrial biogenic emissions, transported by easterly continental flow from around midnight to midday, followed by increased marine influence in the afternoon under sea-breeze flow. From 24 to 26 May, dominant source airmasses advected over the upwelling waters of the Benguela Current could carry marine biogenic emissions, together with anthropogenic pollutants from shipping emissions. From 28 to 30 May, the site was influenced predominantly by marine emissions transported by the westerly oceanic flow.

In summary, three representative regimes were identified in this study, based on airmass sources and meteorological conditions: Period 1 (16 to 23 May and on 27 May) characterized by easterly continental flow and local marine influence; Period 2 (24 to 26 May) characterized by southeasterly coastal flow along the Benguela region; and Period 3 (28 to 30 May) characterized by westerly oceanic flow.

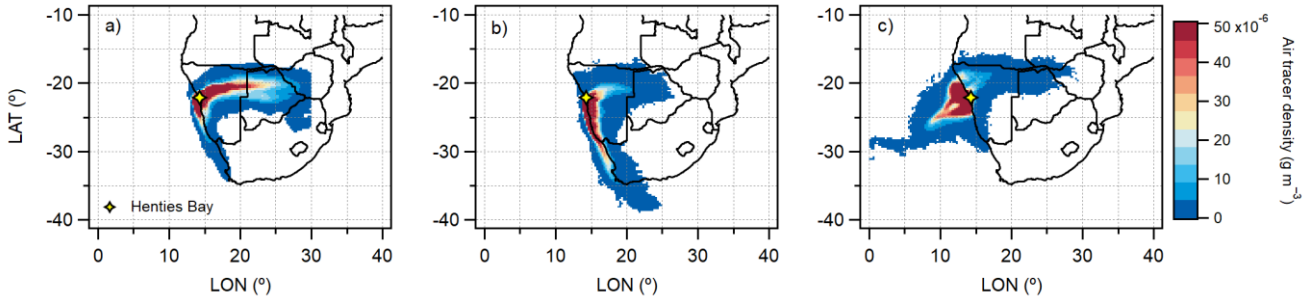


Figure 1. Integrated backward-dispersion fields for simulations from (a) 16–23 May and 27 May, (b) 24 to 26 May, and (c) 28–30 May. The fields illustrate the horizontal footprints of original air parcels transported over the preceding two days before reaching the Henties Bay site (indicated by the yellow marker).

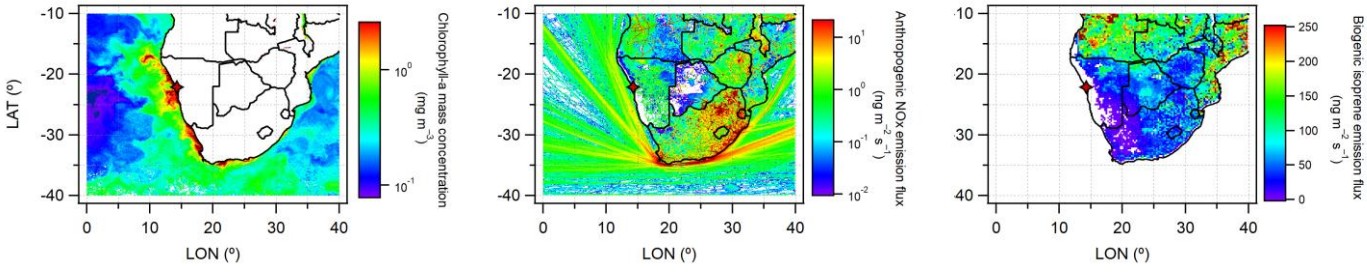


Figure 2. (a) Average mass concentrations of ocean surface chlorophyll-a during the campaign period. (b, c) Average emission fluxes of b) anthropogenic NOx and c) biogenic isoprene for May 2024. Henties bay site location is indicated by the red marker.

https://doi.org/10.5194/egusphere-2026-6260
Preprint. Discussion started: 19 November 2026
© Author(s) 2026. CC BY 4.0 License.

3.2 Source-dependent aerosol characterization

3.2.1 Aerosol number size distribution

Figure 3 presents the aerosol number size distributions obtained by the combination of SMPS (black open circles) and GRIMM (black open triangles) measurements, for the three identified periods in Section 3.1. The corresponding time series of aerosol number size distributions measured by the SMPS and GRIMM are shown in Fig. S4 in the supplement. Median SMPS number size distributions were fitted using a sum of lognormal modes. Period 1 was separated into continental-flow (Fig. 3a) and sea-breeze conditions (Fig. 3b), due to a pronounced diurnal shift in air-mass origin. Period 1 exhibited a wide particle-size range, particularly during the afternoon and evening. Under the continental-flow regime (Fig. 3a), the median distribution was dominated by an accumulation-mode peak centered at 124 nm with a geometric standard deviation of 1.88. Following the development of the local sea-breeze circulation in the afternoon, an Aitken mode appeared with the peak centered at 40 nm, while the accumulation-mode component remained broadly similar (Fig. 3b). The broad distributions observed during Period 1 indicate mixed aerosol populations influenced by both continental outflow and local marine emissions, as reported in previous coastal observations (Dall'Osto et al., 2010; Hilario et al., 2021; Kawana et al., 2022). The dominant accumulation-mode components may reflect the influence of continental pollutants, which may favor particle growth through condensation and coagulation (Dournaux et al., 2025). The enhanced Aiken mode during the afternoon suggests an additional contribution from freshly emitted or formed particles associated with the local sea breeze that brought more marine emissions.

Period 2 exhibited a bimodal structure, characterized by a dominant Aitken-mode peak centered at 57 nm and a secondary accumulation-mode peak centered at 163 nm (Fig. 3c). During Period 2, southeasterly coastal flow transported over the Benguela Current could have brought marine biogenic emissions, which may contribute to new particle formation and subsequent growth within the marine boundary layer (Giorio et al., 2022). The two submicron modes during Period 2 are consistent with previous shipborne and coastal observations under marine biologically active conditions, which reported bimodal aerosol number size distributions with peak diameters at approximately 30–60 nm and 100–200 nm (Dall'Osto et al., 2011; Ueda et al., 2016; Xu et al., 2021; Dournaux et al., 2025). In addition, the southeasterly flow may also have transported shipping-related pollutants along the coast. Previous observations showed that shipping emissions are typically dominated by unimodal number size distributions peaked at ~20–80 nm, depending on fuel sulfur content, engine load, and atmospheric aging (Ausmeel et al., 2019; Yu et al., 2020; Seppälä et al., 2021; Eger et al., 2023). This size range is also consistent with the dominant Aitken-mode peak observed during Period 2. Therefore, the dominant Aitken-mode contribution likely reflects a persistent influence of freshly emitted or formed particles associated with marine and/or shipping sources, whereas the smaller accumulation-mode contribution may represent particles that had undergone growth during coastal transport.

In contrast, Period 3 had the lowest aerosol number concentrations during the campaign (Fig. 3d), reflecting cleaner airmasses associated with westerly oceanic flow, compared to Periods 1 and 2. Period 3 displayed a distinct bimodal structure, dominated by an accumulation-mode peak centered at 192 nm, with a smaller Aitken-mode contribution centered at 65 nm. There was a pronounced minimum near 90 nm between the two modes. This structure resembles a Hoppel minimum, indicating the

https://doi.org/10.5194/egusphere-2026-6260
Preprint. Discussion started: 19 November 2026
© Author(s) 2026. CC BY 4.0 License.



influence of cloud processing during the transport of marine airmasses from open ocean to the coast, as observed in previous studies (Rinaldi et al., 2009; Kawana et al., 2022). Cloud processing can shift aerosol size distributions toward larger diameters through in-cloud reactions, coalescence or coagulation within cloud droplets, and subsequent droplet evaporation. These processes may explain the larger accumulation-mode diameter during period 3 under westerly aged oceanic flow (192 nm) compared with period 2 under coastal marine influence (163 nm). Overall, substantial variability in aerosol number size distributions was observed among different meteorological regimes, reflecting the influence of different aerosol sources (e.g. continental outflow, marine emissions, and shipping) and atmospheric processes (e.g. cloud processing).

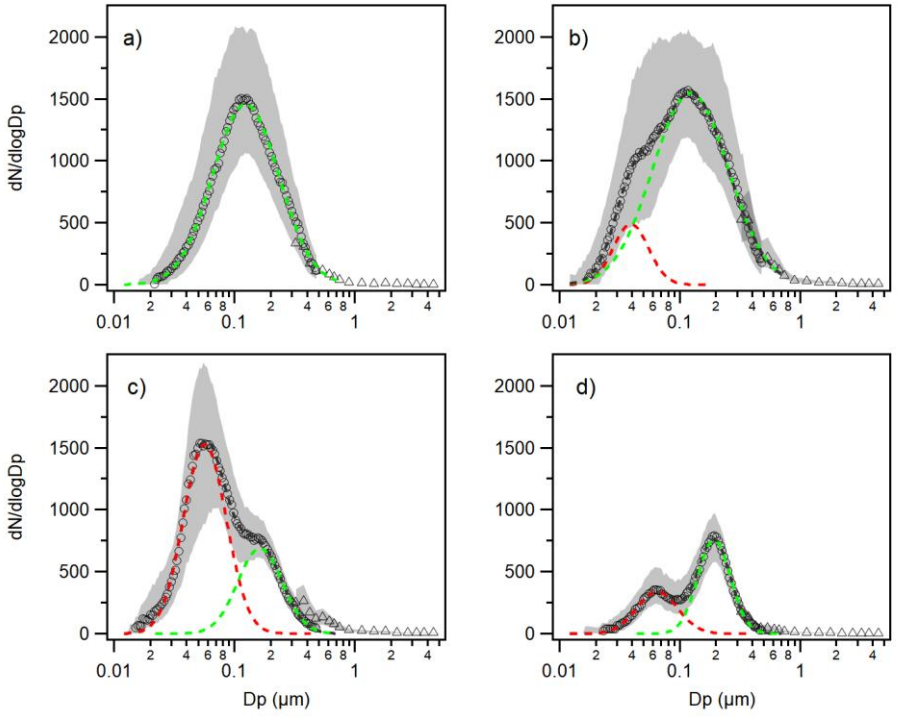


Figure 3. Aerosol number size distributions and lognormal modal fits summarized for a) Period 1, continental flow regime; b) Period 1, sea-breeze regime; c) Period 2; and d) Period 3. Black open circles and triangles show the measured median number size distributions from the SMPS and GRIMM measurements respectively. Grey shading indicates the interquartile range. Colored dashed lines indicate individual fitted lognormal modes for median SMPS number size distributions, and black dashed line represents the total fitted distribution.

3.2.2 Aerosol hygroscopicity

Figure 4 summarizes the *SS* dependence of these hygroscopic parameters for the three identified periods. Since CCN measurements were only available from 22 May onwards, the statistical representation of Period 1 is based on fewer data than the aerosol size distributions discussed above. As a complement, Figure S5 in the supplement shows the time series of aerosol hygroscopic parameters at different *SS* (0.1, 0.2, 0.3, 0.4, and 0.5%), including the N_{CCN}, D_c, CCN activation ratio, and CCN-

https://doi.org/10.5194/egusphere-2026-6260
Preprint. Discussion started: 19 November 2026
© Author(s) 2026. CC BY 4.0 License.

derived hygroscopicity parameter (κ_{CCN}). Substantial variability was observed during the campaign, e.g., at *SS* = 0.3%, N_{CCN} ranged from 58 to 2036 cm^{-3} and κ_{CCN} ranged from 0.08 to 0.58.

For all periods, N_{CCN} generally increased (Fig. 4a), as D_c decreased with increasing *SS* (Fig. 4b), reflecting the activation of progressively smaller particles at higher *SS*. Larger particles preferentially activate as CCN because they reduce the critical supersaturation required for droplet activation by weakening the Kelvin effect (Dusek et al., 2006). Accordingly, the CCN activation ratio increased with *SS* (Fig. 4c). Period 1 exhibited the largest ranges of N_{CCN} across different *SS*. At lower *SS* of 0.1 % and 0.2 %, the D_c was mainly located within the accumulation-mode size range (> 0.1 μm), whereas it shifted towards the Aitken-mode at higher *SS*. Correspondingly, the median N_{CCN} progressively increased from 307 cm^{-3} at SS = 0.1% to 779 cm^{-3} at SS = 0.5%. Compared to Period 1, Period 2 showed smaller ranges of N_{CCN} across different *SS*. The median N_{CCN} progressively increased from 215 cm^{-3} at SS = 0.1% to 619 cm^{-3} at SS = 0.5%, with the median D_c decreasing from 142 to 73 nm. Period 2 was characterized by a dominant Aitken mode and a weaker accumulation mode, while Period 1 showed broad distributions across Aitken and accumulation modes (Figs. 3a-c). Therefore, despite the smaller D_c values, the activation ratio during Period 2 remained generally lower than those during Period 1. Period 3, the cleanest period, exhibited the lowest and least variable N_{CCN} during the campaign. At lower *SS*, the D_c during Period 3 had the lowest ranges, indicating the most efficient activation of accumulation-mode particles. It became comparable to Period 2 at higher *SS*. The median N_{CCN} increased from 236 cm^{-3} at SS = 0.1% to 345 cm^{-3} at SS = 0.3%, and remained nearly constant at higher *SS*, suggesting that most particles within the measured size range were already activated by SS = 0.3%. Despite having the lowest N_{CCN}, Period 3 showed the highest CCN activation ratios across different *SS*. This behavior is consistent with the dominance of accumulation-mode particles (Fig. 3d).

The aerosol hygroscopicity parameter (κ) reflects the ability of aerosol particles to take up water and act as CCN. For all periods, the inferred κ_{CCN} values decreased with increasing *SS* (Fig. 4d), suggesting that smaller particles activated at higher *SS* were, on average, less hygroscopic than the larger particles activated at lower *SS*. Similar *SS*-dependent decreases in κ_{CCN} have been previously reported in other coastal and marine environments, which were commonly attributed to size-dependent aerosol composition, with smaller particles enriched in less-hygroscopic organics (Meng et al., 2014; Cheung et al., 2020; Royer et al., 2023). Period 1 showed the lowest ranges of κ_{CCN} values across different *SS*, indicating broadly less hygroscopic aerosols compared to other two periods. The median κ_{CCN} during Period 1 decreased from 0.31 at SS = 0.1% to 0.11 at SS = 0.5%. Period 2 showed generally higher κ_{CCN} than Period 1, with the median κ_{CCN} decreasing from 0.51 at SS = 0.1% to 0.17 at SS = 0.5%. Periods 3 exhibited the highest ranges of κ_{CCN} values at lower *SS* of 0.1 % and 0.2%, while became comparable to Period 2 at higher *SS*. This behavior indicates that the enhanced hygroscopicity during Period 3 was mainly associated with accumulation-mode particles, whereas the Aitken-mode particles activated at higher *SS* had hygroscopicity similar to those during Period 2.

Figure 5 shows the comparison between κ_{CCN} at SS = 0.3% and the composition-derived hygroscopicity parameter, κ_{chem}, which can provide further insight into the role of aerosol mixing state in observed varying aerosol hygroscopicity. The κ_{chem} values were estimated from bulk ToF-ACSM-X chemical composition assuming internally mixed aerosols (see Sect. 2.3.2).

https://doi.org/10.5194/egusphere-2026-6260
Preprint. Discussion started: 19 November 2026
© Author(s) 2026. CC BY 4.0 License.

Figure S6 in the supplement shows the diurnal profiles of average fractional contributions of different submicron chemical compositions for the three identified periods, providing additional support for the period-dependent behavior of κ_{CCN}. During Period 1, the κ_{chem} values are generally higher than κ_{CCN}, suggesting that the internal-mixing assumption likely overestimated the effective CCN activity of ambient aerosols. In contrast, there is a closer agreement between κ_{CCN} and κ_{chem} during Periods 2 and 3. This discrepancy indicates a greater degree of external mixing during Period 1 than Periods 2 and 3, when the site was influenced by mixed continental outflow and marine air masses. Such external mixing would explain the relatively low κ_{CCN} values observed during Period 1, although fractional compositions were similar between Periods 1 and 2 (Fig. S6 in the supplement). Reductions in κ values after continental aerosols externally mix with marine aerosols have also been reported in previous coastal and marine studies (Wex et al., 2010; Xu et al., 2021).

As shown in Fig. S6 in the supplement, Period 3 had enhanced sulfate fractions ($sulfate_{average}$ = 33.7%) accompanied by ammonium ($ammonium_{average}$ = 16.1%), compared to Period 1 ($sulfate_{average}$ =27.8%; $ammonium_{average}$ =11.3%) and Period 2 ($sulfate_{average}$ =25.9%; $ammonium_{average}$ =11.5%). As indicated by a Hoppel minimum structure in aerosol number size distributions (Fig. 3d), the aerosols during Period 3 may have undergone cloud processing, when transporting from open ocean to the coastal site. Non-precipitating cloud processing preferentially activates accumulation-mode particles into droplets, whereas Aitken-mode particles remain mostly interstitial. Within cloud droplets, the aqueous-phase oxidation of dissolved SO_2 can produce sulfate, leading to larger and more internally mixed accumulation-mode aerosols after droplet evaporation. Previous studies in marine and continental environments have shown that cloud processing can enhance sulfate contents at larger particle sizes (Dall'Osto et al., 2010; Henning et al., 2014; Ervens et al., 2018; Xu et al., 2020). Therefore, the enhanced sulfate fraction observed during Period 3 was likely more associated with the accumulation mode, contributing to the higher κ_{CCN} values at low *SS*. In contrast, Aitken-mode particles were less likely to have experienced repeated droplet activation during cloud processing and may have originated from similar secondary aerosol formation and growth processes in Periods 2 and 3. The production of ultrafine particles can be driven by the condensation of both organic and inorganic vapors (Xu et al., 2024). Consequently, the κ_{CCN} values at higher *SS*, where the inferred D_c shifted towards the Aitken-mode size, were more comparable between Periods 2 and 3.

Overall, the CCN activity at Henties Bay was controlled by the combined effects of aerosol size distribution, chemical composition, and mixing state under different airmass source conditions. The aerosol number size distribution primarily determined the magnitude of N_{CCN}, while differences in compositions and mixing states contributed to the observed source-dependent κ_{CCN} and activation behavior.

https://doi.org/10.5194/egusphere-2026-6260
Preprint. Discussion started: 19 November 2026
© Author(s) 2026. CC BY 4.0 License.

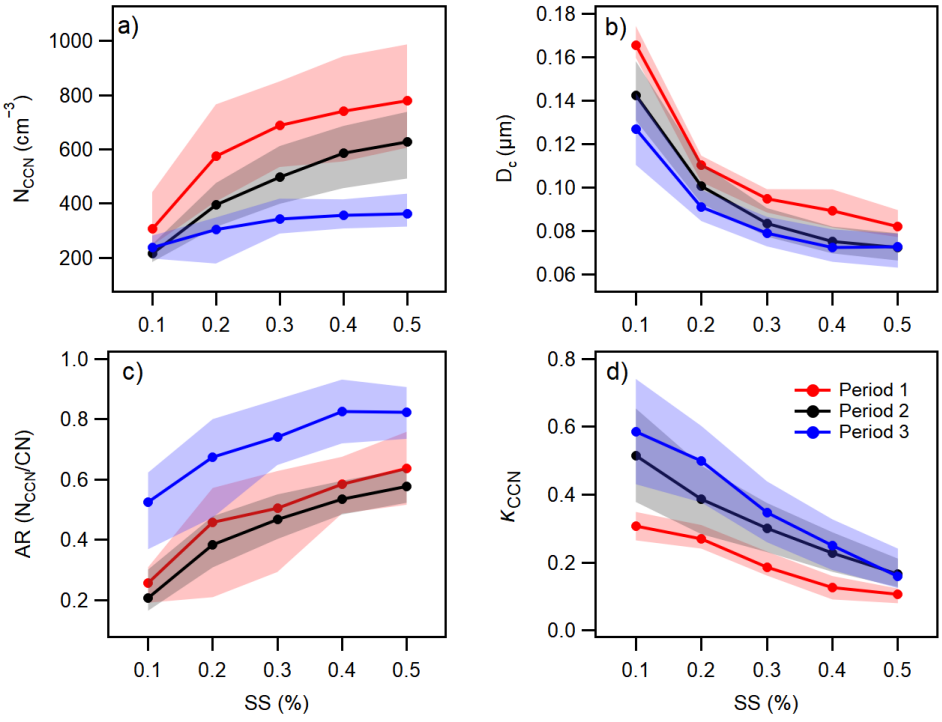


Figure 4. Supersaturation dependence of (a) CCN number concentration, N_{CCN}, (b) activation diameter, D_c, (c) CCN activation ratio (AR= N_{CCN}/CN), where CN is the particle number concentration integrated from the SMPS size distributions, and (d) CCN-derived hygroscopicity parameter, κ_{CCN}, for the three identified periods. Markers indicate median values, and shaded areas represent the interquartile range.

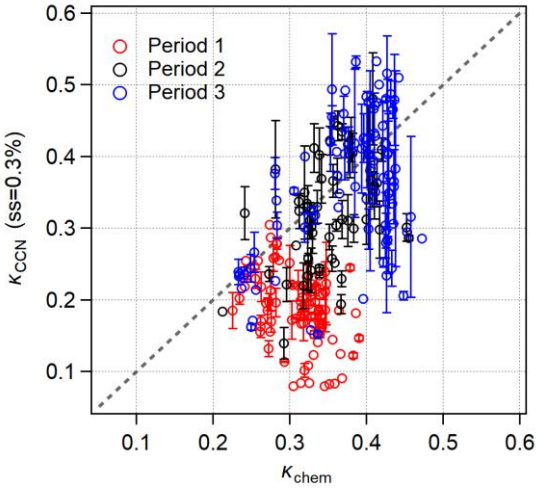


Figure 5: The comparison between κ_{CCN} derived from size-resolved CCNc measurements and κ_{chem} estimated from the ACSM compositions. The κ_{CCN} values were averaged to the ACSM time step, and the bars represent the standard deviation.

https://doi.org/10.5194/egusphere-2026-6260
Preprint. Discussion started: 19 November 2026
© Author(s) 2026. CC BY 4.0 License.

3.3 Fog occurrence and characterization

3.3.1 Fog microphysics

Fog events were defined when the following criteria were met simultaneously: RH exceeding 95 %, N_d greater than 5 cm^{-3}, and LWC greater than 0.01 g m^{-3}. Intervals between individual fog events were required to include at least 3 consecutive hours of a fog-free period. During the campaign, seven fog events were observed, as summarized in Table S2 in the supplement. No fog events occurred during Period 1, which was dominated by easterly continental outflow with afternoon sea-breeze influence. E3-E5 (24–26 May) occurred during Period 2 under southeasterly coastal flow along the Benguela region, whereas E6-E7 (28–29 May) occurred during Period 3 under westerly oceanic flow. E1-E2 (14–15 May) occurred during the transitional period at the beginning of the campaign, when the site was shifting from coastal flow toward stronger easterly continental influence.

The event-median values of N_d, LWC, and R_{eff} varied from 13 to 69 cm^{-3}, 0.02 to 0.21 g m^{-3}, and 6.7 to 10.2 µm, respectively, with event-maximum values reaching 139 cm^{-3}, 0.90 g m^{-3}, and 13.9 µm (Fig. 6). The N_d levels observed at Henties Bay are comparable to those reported for clean coastal and marine fog, which typically range from 5 to 100 cm^{-3} (Isaac et al., 2020; Duplessis et al., 2021) but are substantially lower than those reported for more polluted coastal fog, where mean N_d values are typically around 200–300 cm^{-3} (Liu et al., 2020; Tsai et al., 2021). The LWC was generally below 0.1 g m^{-3}, consistent with values reported for coastal fog, including previous measurements at Henties Bay in September 2017 (Wang et al., 2021; Weston et al., 2022). The E5 on 26 May is distinct, exhibiting substantially higher LWC than other events, which overlaps with values reported for thick fog and stratus clouds (Costabloz et al., 2025; Wu et al, 2025).

Example time series of fog microphysical properties are shown in Figs. S7 and S8 in the supplement. For E3-E5 (Period 2 fog events), continuous nocturnal fog was observed. The full local evolution, including the formation, development, mature-stage, and dissipation, was captured at the site (Fig. S7 in the supplement). These events varied in both duration and microphysics. Their median droplet size distributions were generally broad and bimodal, with a smaller-droplet mode around 6 µm and a larger-droplet mode ranging from ~ 13 µm to above 20 µm (Fig. 7a). Among these events, E5 showed the broadest distribution and the strongest contribution from larger droplets, with droplet diameter extending to ~ 40 µm. This is consistent with its substantially higher LWC and larger R_{eff}, indicating more efficient droplet growth and a more developed fog during this event. Satellite retrievals show largely clear-sky conditions over most of the ocean and inland areas during 24-26 May (Fig. S9 in the supplement), suggesting that E3-E5 were likely small-scale fog patches that formed locally.

In contrast, the other events (E1, E2, E6, and E7) were intermittent and generally had longer duration periods spanning both day- and night-time (Fig. S8 in the supplement). These events showed stronger temporal variability in fog microphysical properties within individual event period. Their median droplet size distributions were broadly similar, with droplet diameter extending to ~ 35 µm and two comparable modes near 6 and 20 µm (Fig. 7b). The E7 featured the lowest N_d and LWC, whereas E1, E2, and E6 showed broadly comparable ranges of microphysical properties. Satellite retrievals show widespread fog and low-level cloud cover over most of the ocean and inland areas on these fog days (Fig. S9 in the supplement), suggesting that these fog events were likely advected marine stratus clouds that lowered to the surface intermittently.

https://doi.org/10.5194/egusphere-2026-6260
Preprint. Discussion started: 19 November 2026
© Author(s) 2026. CC BY 4.0 License.

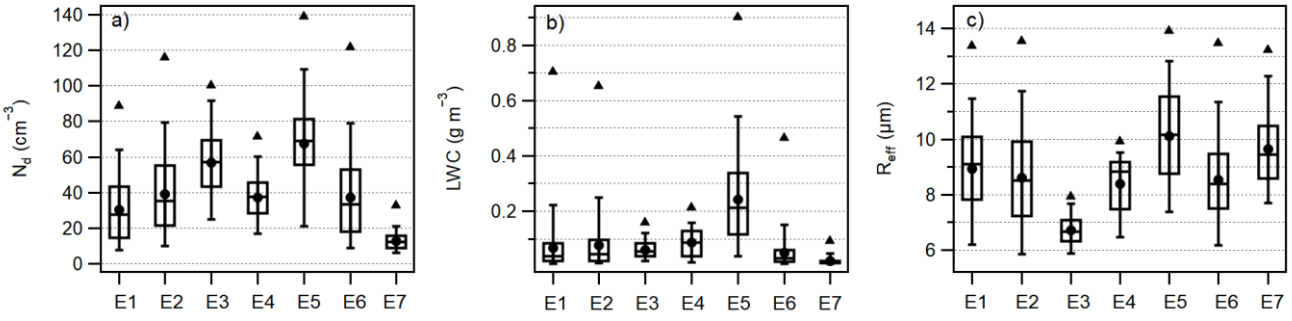


Figure 6. The summary of a) N_d, b) LWC, and c) R_{eff} for observed fog events. The circle makers, lines, triangle makers, boxes and whiskers represent median, average, maximum, 25 to 75 percentile range, and 5 to 95 percentile range.

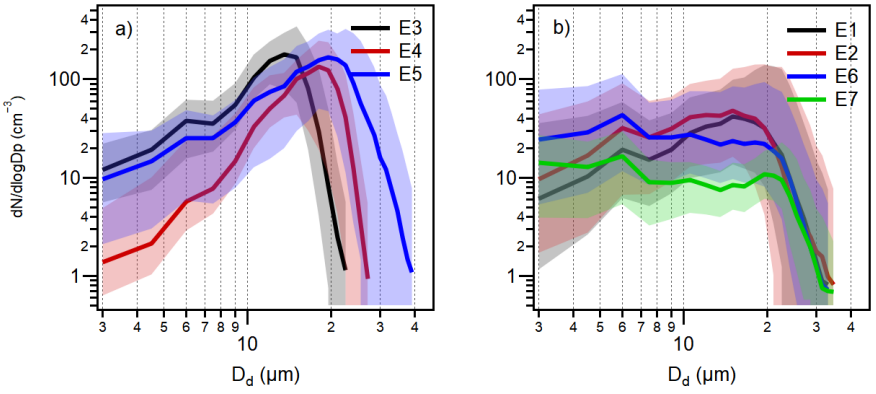


Figure 7. The droplet number size distributions for observed fog events. The lines and shades represent median and 5 to 95 percentile range.

3.3.2 Relationship between fog and pre-fog aerosols

The average N_a in the last hour before the start of each fog event was defined as pre-fog N_a. Figure 8 shows the relationship between peak N_d and pre-fog N_a for six fog events (E2 to E7). E1 was excluded because no pre-fog aerosol observations were available. Excluding E5, a strong positive correlation was found between peak N_d and pre-fog N_a (R^2=0.92, p=0.009), indicating pre-fog aerosols influenced droplet activation and N_d. E5 exhibited stronger aerosol activation than the other events. Positive relationships between peak N_d and pre-fog aerosol abundance have also been reported in previous fog studies (Duplessis et al., 2021; Liu et al., 2025). It is noted that pre-fog aerosols measured at the site may not exactly represent the aerosols at the location of initial fog formation, particularly for fog events associated with advected marine stratus. Nevertheless, the observed relationship suggests that pre-fog measurements may provide a reasonable proxy for the aerosol population relevant to initial fog droplet activation.

Based on this result, pre-fog CCNc measurements were used to estimate the effective supersaturation (SS_{CCN}) during fog. Due to incomplete observation data of CCNc, only five events (E3 to E7) were available for the SS_{CCN} estimation. Since the inferred

https://doi.org/10.5194/egusphere-2026-6260
Preprint. Discussion started: 19 November 2026
© Author(s) 2026. CC BY 4.0 License.

SS_{CCN} values were below the lowest CCNc SS set point (0.1 %), uncertainties may be introduced by linear extrapolation to lower supersaturations. Furthermore, this SS_{CCN} estimation assumes that the observed N_d primarily reflects adiabatic processes of activation and condensation, whereas non-adiabatic processes such as collision-coalescence and sedimentation are ignored (Mazoyer et al., 2022). If such processes have reduced N_d after activation, the inferred SS_{CCN} would represent a lower-limit estimate of the effective supersaturation.

Example time series of inferred SS_{CCN} in fog events are shown in Figs. S7 and S8 in the supplement. The event-median SS_{CCN} values ranged from 0.006 % to 0.043 %, with event-maximum values ranging from 0.018 % to 0.085 % (Fig. 9a). These values are mostly comparable to the low supersaturations reported for coastal fog (< 0.05%), rural fog (mostly below 0.04%), and urban polluted fog (0.01% to 0.05%) (Shen et al., 2018; Duplessis et al., 2021; Wainwright et al., 2021). The E5 exhibited the highest SS_{CCN}, which exceeded the upper range reported for coastal fog (Duplessis et al., 2021) and approached the lower end of typical marine boundary-layer clouds (0.10% – 0.50%) (Gong et al., 2023). This is consistent with the stronger aerosol activation for E5 compared to the other events (Fig. 8).

The SS_{CCN} values were generally higher during E3-E5 (Period 2 fog events) than during E6-E7 (Period 3 events). This difference may be partly associated with the lower temperatures observed during Period 2 (Fig. 9b), because colder air has a lower equilibrium saturation vapor pressure and favors the development of supersaturated conditions for a given water-vapor content (Rogers and Yau, 1989). In addition, the fog evolution during E3-E5 was closely associated with temperature changes. As shown in Fig. S7 in the supplement, the temperature presented a generally decreasing trend during fog period. Such cooling could initially increase excess water vapor pressure and SS_{CCN}, thereby activating additional smaller particles (Liu et al., 2025). This process resulted in a short period increase in N_d and LWC, together with a reduction in droplet size. Despite continued cooling, this response was rapidly damped, likely because newly activated droplets enhanced the condensational sink and competed for water vapor. The sustained cooling after fog formation is unlikely solely due to local radiative cooling and may instead reflect the advection of cooler marine air that had undergone radiative cooling in nearby clear-sky regions (Fernando et al., 2021). Such cold-air advection could maintain or enhance supersaturation at Henties Bay and thereby promote continued aerosol activation. In contrast, temperatures were generally higher and more stable during E6-E7, with no clear correlation between the temporal variations in temperature and SS_{CCN} (Fig. S8 in the supplement). These differences further suggest that E3-E5 were likely locally formed fog, which could be influenced by both radiative and advective cooling. By comparison, E6 and E7 were likely less controlled by local cooling-induced activation and were instead more influenced by the prior activation history associated with advected marine stratus.

Overall, the observations presented variable SS_{CCN} levels among events, which, together with differences in pre-fog aerosol abundance, likely contributed to the observed variability in aerosol activation behavior and fog microphysical properties. The higher SS_{CCN} values during E3-E5 (Period 2 fog events) may be linked to lower temperatures and sustained cooling, whereas E6-E7 (Period 3 events) suggest weaker local activation. In the next section, we will discuss the role of meteorological conditions in controlling fog occurrence, local SS_{CCN} levels, and thus fog microphysical properties.

https://doi.org/10.5194/egusphere-2026-6260
Preprint. Discussion started: 19 November 2026
© Author(s) 2026. CC BY 4.0 License.

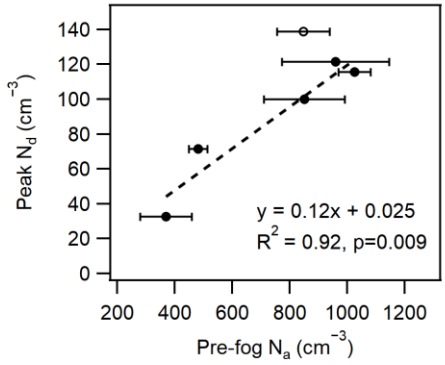


Figure 8. Peak N_d value for available fog event versus averaged pre-fog N_a in the last hour before the fog event. E5 is shown as an open circle, which is deviated from the relationship observed for the other events (solid circle). The dashed line represents the linear fitting to the other events.

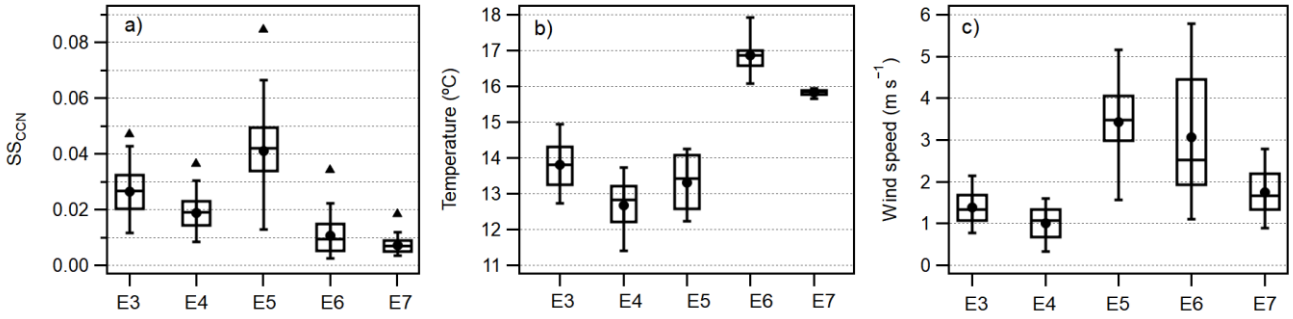


Figure 9. The summary of a) inferred SS_{CCN} for available fog events, along with the corresponding b) temperature and c) wind speed during fog periods. The circle makers, lines, triangle makers, boxes and whiskers represent median, average, maximum, 25 to 75 percentile range, and 5 to 95 percentile range.

3.3.3 The role of synoptic-scale meteorological conditions

Figure 10 summarizes the mean vertical structure of the regional atmosphere along a zonal cross-section at the site latitude (22° S) at 3:00 UTC for the three identified periods, including temperature, specific humidity, RH, and wind fields. The corresponding meridional cross-sections along the site longitude (14.26° E) are shown in Fig. S10 in the supplement. During Period 1, the coastal region was influenced by pronounced easterly continental flow, which blew over the Great Escarpment and descended toward the coastal surface layer (Figs. 10a, d, and g). The associated adiabatic warming and dry-air advection likely displaced the shallow marine boundary layer, resulting in a warm and dry condition along the coast. Such conditions are consistent with bergwind-type situations along the west coast of southern Africa, which are typically characterized by warm, dry, and strong offshore winds and favor the dissipation of fog and low stratus clouds (Tlhalerwa et al., 2012; Ndarana et al., 2018). This is consistent with the absence of fog during Period 1 and with the largely clear-sky conditions over the ocean and inland areas indicated by satellite retrievals of daily fog and low clouds (Fig. S9 in the supplement).

https://doi.org/10.5194/egusphere-2026-6260
Preprint. Discussion started: 19 November 2026
© Author(s) 2026. CC BY 4.0 License.

During Period 2, the easterly component weakened (Figs. 10b, e, and h), and the low-level circulation became strongly influenced by southerly coastal advection (Fig. S10 in the supplement). In contrast to Period 1, the easterly subsiding wind did not fully penetrate to the surface at the coast. A warm and dry layer developed above a cooler and moister coastal boundary layer influenced by the cold Benguela Current. The resulting capping inversion would limit the entrainment of warm and dry free-tropospheric air and confine moisture within the shallow coastal boundary layer. Under these conditions, nocturnal radiative cooling may have brought the near-surface layer to saturation and initiated local fog formation. As discussed in Sect. 3.3.2, the continued temperature decrease after fog formation suggests that the advection of cooler marine air also contributed to the cooling and influenced subsequent fog evolution. These events therefore likely involved a combination of radiative and advective processes. A similar case has been described for the California coast, where dense local fog can form after a hot and dry offshore flow relaxes and caps a cool and moist marine boundary layer at the surface (Leipper, 1994). Hipler et al. (2026) also reported a related mechanism for a Namibian fog event associated with advected stratus, where warm and dry easterly advection formed an inversion and promoted the lowering of marine stratus. In that case, however, the inversion was located substantially higher. By contrast, the much lower capping inversion in this study likely limited the vertical development of the fog layer. These observations highlight that such synoptic situations do not only dissipate coastal fog and low clouds as previously reported (Adebiyi and Zuidema 2018), but may also regulate their vertical position and extent, and even facilitate local fog formation at or near the coast.

The inversion was particularly pronounced during E5 on 26 May (Fig. S11 in the supplement), which may have more effectively suppressed entrainment of warm and dry air from aloft, and maintained the fog after its formation. Therefore, E5 had the longest duration among the locally formed fog events. The higher SS_{CCN} inferred for E5 may have resulted from enhanced mechanical turbulence associated with stronger near-surface winds (Fig. 9c). Such conditions could increase moisture and heat exchange within the shallow layer, promoting supersaturation development, droplet activation, and condensational growth of droplets. This mechanism may contribute to the higher N_d, LWC, and R_{eff} observed in E5 compared with other locally formed fog events (E3-E4). Previous studies have also indicated that fog liquid water path and fog layer development can be sensitive to wind speed and turbulence (Román-Cascón et al., 2019; Dione et al., 2023).

During Period 3, the easterly offshore flow largely disappeared, and the lower troposphere became substantially more humid from the ocean toward the inland Namibia (Figs. 10c, f, and i). Although a weak inversion was still present, it was more likely a marine boundary-layer capping inversion associated with oceanic advection and subsidence. The deeper moist layer allows for the inland penetration of marine boundary-layer air and is consistent with the advection of low-level stratus from the ocean. The Period 3 fog events (E6-E7) were therefore likely dominated by the inland advection of marine stratus. This is also consistent with the relatively high wind speeds observed during these events, which would favor the inland transport (Fig. 9c). Concurrent ceilometer observations using a Vaisala CL31 at the coastal Swakopmund site, approximately 70 km southeast of the Henties Bay site, provide additional evidence for this interpretation (Fig. S12 in the supplement). Details of the Swakopmund site location and instrument specifications are provided in Malik et al. (2026). Very low cloud bases were detected at the Swakopmund site during E6-E7, indicating the presence of a low-lying cloud layer extending along the

https://doi.org/10.5194/egusphere-2026-6260
Preprint. Discussion started: 19 November 2026
© Author(s) 2026. CC BY 4.0 License.

Namibian coast. This suggests that E6-E7 were associated with the lower part or base of large-scale advected marine stratus. The intermittent pattern of these fog events may reflect the lifting and lowering of cloud base during the fog life cycle (Malik et al., 2026). This advected stratus regime would be expected to have relatively low local supersaturation. Droplets were likely already activated upstream over the ocean. These pre-existing droplets would provide an efficient condensation sink and consume excess water vapor produced locally, buffering local supersaturation at low values (Pinsky and Khain, 2020). Moreover, if the advected stratus was approximately adiabatic, its LWC would be close to zero at cloud base and increase with height. The low LWC observed during E6-E7 is consistent with the site sampling the lower part or base of advected stratus. Therefore, the lower SS_{CCN} and LWC values were observed for E6-E7 compared with E3-E5 (Figs. 6 and 9).

Overall, these results indicate that synoptic-scale meteorology played a key role in modulating fog occurrence, formation pathways, and supersaturations at Henties Bay. In combination with the aerosol analysis, these results suggest that meteorology primarily controlled whether and how fog formed, whereas pre-fog aerosol properties further modulated fog microphysical characteristics.

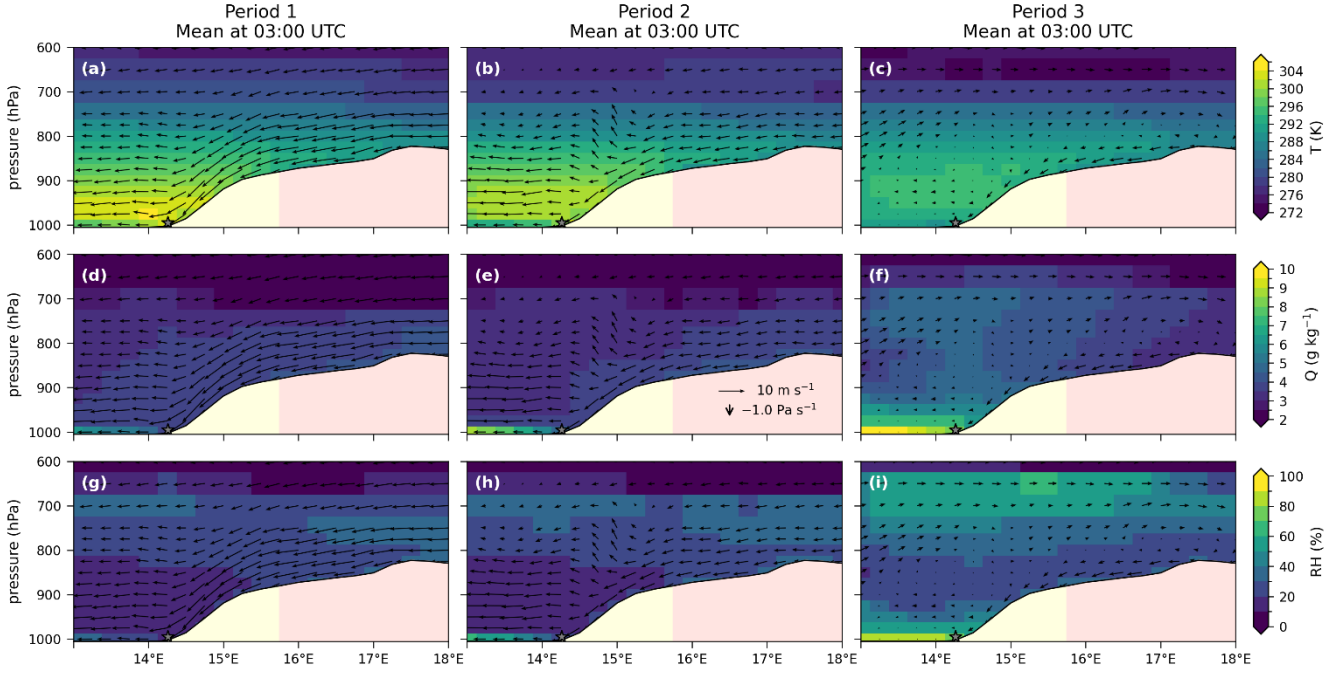


Figure 10. Regional atmospheric structure at Henties Bay (grey star) in latitudinal curtain plots at 22◦S, which was analyzed from ERA5. The columns represent mean vertical structure of the regional atmosphere at 3:00 UTC for the three identified periods. Shading shows temperature (T; a–c), specific humidity (q; d–f), and relative humidity (RH; g–i). Vectors represent the zonal wind component and vertical velocity (ω); negative ωdenotes upward motion. Reference vectors corresponding to 10 m $s^{-1}$and 1.0 Pa s^{-1} are shown in panel (e).

https://doi.org/10.5194/egusphere-2026-6260
Preprint. Discussion started: 19 November 2026
© Author(s) 2026. CC BY 4.0 License.

4 Conclusions

This study investigated source-dependent aerosol properties and the coupled influences of meteorological conditions and aerosols on fog occurrence, formation pathways, and microphysics in coastal Namibia. Coordinated measurements of aerosols, fog droplets, and meteorology were conducted at Henties Bay in May 2024, during the first intensive AEROFOG campaign. These observations were interpreted together with backward-dispersion simulations, satellite retrievals of fog and low clouds, and regional atmospheric structures derived from ERA5 reanalysis.

Three distinct airmass regimes were identified, based on backward-dispersion simulations. Period 1 was dominated by easterly continental outflow, with the development of local sea breeze in the afternoon. This regime exhibited broad aerosol number size distributions spanning the Aitken and accumulation modes and the greatest variability in N_{CCN}. Nevertheless, it showed the lowest range of κ_{CCN} under the combined influence of continental and marine airmasses, likely due to a higher degree of external mixing than Periods 2 and 3. Period 2 was dominated by southeasterly coastal flow along the Benguela upwelling region, characterized by dominant Aitken-mode particles and moderate hygroscopicity. Period 3 was associated with westerly oceanic flow and exhibited the lowest aerosol number concentrations but the highest CCN activation fractions. The aerosol size distributions were dominated by an accumulation mode and presented a pronounced Hoppel minimum structure, indicating that the aerosols had likely undergone cloud processing during transport from the open ocean to the coast. Cloud-processed, sulfate-enriched accumulation-mode particles likely led to the highest range of κ_{CCN} at low SS during Period 3.

During the campaign, seven fog events were identified. Their event-median N_d, LWC, and R_{eff} varied from 13 to 69 cm^{-3}, 0.02 to 0.21 $g\,m^{-3}$, and 6.7 to 10.2 µm, respectively. The generally low N_d and LWC values are comparable to those reported for clean coastal and marine fog (Isaac et al., 2020; Duplessis et al., 2021; Wang et al., 2021; Weston et al., 2022). The E5 on 26 May was distinct, exhibiting substantially higher LWC than the other events, overlapping with those reported for thick fog and stratus clouds (Costabloz et al., 2025; Wu et al, 2025). The locally formed fog (E3-E5) differed in duration and microphysical properties between events. By comparison, fog events associated with the advected marine stratus showed stronger temporal variability within individual events, and broadly comparable ranges of event-level microphysical properties.

Peak N_d was positively correlated with pre-fog N_a, indicating that aerosol abundance influenced the number of activated fog droplets. It is also likely that pre-fog aerosols were sufficiently representative for the aerosol population at the upstream location where fog initially formed, particularly for fog events from lowering marine stratus. Based on this relationship, the SS_{CCN} was estimated from pre-fog CCN measurements. Event-median SS_{CCN} ranged from 0.006 % to 0.043 %, while event-maximum values reached 0.085 %. Locally formed fog generally exhibited higher inferred SS_{CCN} than fog events from lowering marine stratus. E5 was characterized by the highest SS_{CCN}, thus deviating from the peak N_d-N_a relationship among the other events.

This study indicates that fog occurrence and formation pathways were primarily governed by synoptic-scale meteorology. During Period 1, pronounced easterly continental flow descended across the Great Escarpment and transported warm and dry air toward the coast. The resulting bergwind-type conditions displaced the shallow marine boundary layer, together with the

https://doi.org/10.5194/egusphere-2026-6260
Preprint. Discussion started: 19 November 2026
© Author(s) 2026. CC BY 4.0 License.

low aerosol κ_{CCN}, and would suppress fog formation. During Period 2, the easterly flow weakened and did not fully penetrate to the surface. A cool and moist coastal boundary layer, maintained by the cold Benguela Current, was capped by a warmer and drier layer. This structure confined moisture near the surface and limited entrainment from aloft, allowing nocturnal cooling to produce local fog (E3-E5). The advection of cooler marine air also contributed to the continued cooling and influenced subsequent fog evolution. These events therefore likely involved a combination of radiative and advective processes. The particularly strong capping inversion during E5 likely reduced dry-air entrainment, and stronger near-surface winds may also have enhanced mechanical turbulence and moisture exchange within the shallow layer. This mechanism favored supersaturation development, aerosol activation, and condensational droplet growth. In contrast, Period 3 was characterized by a deeper marine-influenced moist layer and widespread fog and low-cloud occurrence over the ocean. The fog events (E6-7) were therefore attributed primarily to the inland advection of marine stratus. Their relatively low local SS_{CCN} is consistent with droplets having been activated upstream and subsequently providing an efficient condensation sink that buffered additional supersaturation near the site. Their relatively low LWC was also consistent with Henties Bay intermittently sampling the lower part or base of advected stratus. Our findings refine the regional picture established by previous studies (Andersen et al., 2019, 2020; Hipler et al., 2026), which identified marine advection and low-stratus transport as important controls on Namib fog occurrence, by showing that fog can also develop locally under coupled radiative-advective forcing. Fog microphysical properties at Henties Bay also depended on formation pathways.

Overall, our results highlight the importance of aerosol sources and atmospheric processes (e.g. cloud processing) in controlling aerosol properties. This supports recent work emphasizing the need for region- and mixing-state-aware representations of aerosol hygroscopicity rather than uniform internally mixed parameterizations (Deshmukh et al., 2026). Synoptic-scale meteorology primarily determines fog occurrence and formation pathways at Henties Bay. Aerosol abundance and CCN ability can modulate fog microphysics, while aerosol alone may not account for the observed variability in fog development when meteorological forcing differs such as inversion strength and turbulence. These observations provide unique quantitative constraints on aerosol properties and fog microphysics under contrasting coastal meteorological regimes. Extending such coordinated observations across seasons would establish the climatological frequency of the identified regimes and provide stronger constraints for aerosol-aware microphysics scheme and fog microphysics over Namibia and other similar coastal environments.

https://doi.org/10.5194/egusphere-2026-6260
Preprint. Discussion started: 19 November 2026
© Author(s) 2026. CC BY 4.0 License.

Code and data availability

AEROFOG ground-based campaign data are available from the AEROFOG AERIS data center: https://aerofog.aeris-data.fr/catalogue/ (last access: 18 November 2026).

Supplement link

The link to the supplement will be included by Copernicus, if applicable.

Author contributions

PF designed the research; CY, VM, HA, AR, HH, BL, DTQ, KWF, LP, MA, CG, MC, MF, HAM, SJP and PF supported and performed field experiments; HW, CY, AR and DTQ prepared in-situ datasets; HA provided the satellite dataset; HW and CY performed NAME analysis; HW analyzed combined datasets and led the manuscript writing.

Competing interests

Paola Formenti and Hendrik Andersen are associate editors of the special issue.

Acknowledgements

The whole AEROFOG team members, including Sylvain Triquet, Clarissa Baldo, and Karine Desboeufs, are thanked for their thorough field work before, during and after the deployment. We thank Frank Göttsche and Axel Göbel for the maintenance of the CL31 instrument and the support in data acquisition, and Anja v.d. Plas and her colleagues from the Ministry of Fisheries and Marine Resources (Swakopmund, Namibia) for the support and for hosting it. The NAME group in the UK Met Office are thanked for their instructions on backward simulations.

Financial support

This research has been supported by Agence Nationale de la Recherche (ANR, grant no. ANR-22-CE92-0051) within the project Aerosols and fog in southern Africa: processes and impact on biogeochemistry (AeroFog).

https://doi.org/10.5194/egusphere-2026-6260
Preprint. Discussion started: 19 November 2026
© Author(s) 2026. CC BY 4.0 License.

References

Adebiyi, A. A. and Zuidema, P.: Low Cloud Cover Sensitivity to Biomass-Burning Aerosols and Meteorology over the Southeast Atlantic, J. Climate, 31, 4329–4346, https://doi.org/10.1175/JCLI-D-17-0406.1, 2018.

Andersen, H. and Cermak, J.: First fully diurnal fog and low cloud satellite detection reveals life cycle in the Namib, Atmos. Meas. Tech., 11, 5461–5470, https://doi.org/10.5194/amt-11-5461-2018, 2018.

Andersen, H., Cermak, J., Solodovnik, I., Lelli, L., and Vogt, R.: Spatiotemporal dynamics of fog and low clouds in the Namib unveiled with ground- and space-based observations, Atmospheric Chemistry and Physics, 19, 4383–4392, https://doi.org/10.5194/acp-19-4383-2019, 2019.

Andersen, H., Cermak, J., Fuchs, J., Knippertz, P., Gaetani, M., Quinting, J., Sippel, S., and Vogt, R.: Synoptic-scale controls of fog and low-cloud variability in the Namib Desert, Atmospheric Chemistry and Physics, 20, 3415–3438, https://doi.org/10.5194/acp-20-3415-2020, 2020.

Ausmeel, S., Eriksson, A., Ahlberg, E., and Kristensson, A.: Methods for identifying aged ship plumes and estimating contribution to aerosol exposure downwind of shipping lanes, Atmos. Meas. Tech., 12, 4479–4493, https://doi.org/10.5194/amt-12-4479-2019, 2019.

Baumgardner, D.: An analysis and comparison of five water droplet measuring instruments, J. Appl. Meteorol., 22, 891–910, https://doi.org/10.1175/1520-0450(1983)022<0891:AAACOF>2.0.CO;2, 1983.

Benas, N., Solodovnik, I., Stengel, M., Hüser, I., Karlsson, K.-G., Håkansson, N., Johansson, E., Eliasson, S., Schröder, M., Hollmann, R., and Meirink, J. F.: CLAAS-3: the third edition of the CM SAF cloud data record based on SEVIRI observations, Earth Syst. Sci. Data, 15, 5153–5170, https://doi.org/10.5194/essd-15-5153-2023, 2023.

Boutle, I., Price, J., Kudzotsa, I., Kokkola, H., and Romakkaniemi, S.: Aerosol–fog interaction and the transition to well-mixed radiation fog, Atmos. Chem. Phys., 18, 7827–7840, https://doi.org/10.5194/acp-18-7827-2018, 2018.

Brown, A., Milton, S., Cullen, M., Golding, B., Mitchell, J., and Shelly, A.: Unified Modeling and Prediction of Weather and Climate: A 25-Year Journey, B. Am. Meteorol. Soc., 93, 1865–1877, https://doi.org/10.1175/bams-d-12-00018.1, 2012.

Canagaratna, M. R., Jimenez, J. L., Kroll, J. H., Chen, Q., Kessler, S. H., Massoli, P., Hildebrandt Ruiz, L., Fortner, E., Williams, L. R., Wilson, K. R., Surratt, J. D., Donahue, N. M., Jayne, J. T., and Worsnop, D. R.: Elemental ratio measurements of organic compounds using aerosol mass spectrometry: characterization, improved calibration, and implications, Atmos. Chem. Phys., 15, 253–272, https://doi.org/10.5194/acp-15-253-2015, 2015.

Cheung, H. C., Chou, C. C.-K., Lee, C. S. L., Kuo, W.-C., and Chang, S.-C.: Hygroscopic properties and cloud condensation nuclei activity of atmospheric aerosols under the influences of Asian continental outflow and new particle formation at a coastal site in eastern Asia, Atmos. Chem. Phys., 20, 5911–5922, https://doi.org/10.5194/acp-20-5911-2020, 2020.

Copernicus Climate Change Service (C3S): Ocean colour from 1997 to present derived from satellite observations, Climate Data Store (CDS) [data set], https://doi.org/10.24381/cds.f85b319d, 2019, last access: 16 July 2026.

https://doi.org/10.5194/egusphere-2026-6260
Preprint. Discussion started: 19 November 2026
© Author(s) 2026. CC BY 4.0 License.

Copernicus Atmosphere Monitoring Service (CAMS): CAMS global emission inventories, Atmosphere Data Store (ADS) [data set], https://doi.org/10.24381/1d158bec, 2020, last access: 16 July 2026.

Costabloz, T., Burnet, F., Lac, C., Martinet, P., Delanoë, J., Jorquera, S., and Fathalli, M.: Vertical profiles of liquid water content in fog layers during the SOFOG3D experiment, Atmos. Chem. Phys., 25, 6539–6573, https://doi.org/10.5194/acp-25-6539-2025, 2025.

Dall'Osto, M., Ceburnis, D., Martucci, G., Bialek, J., Dupuy, R., Jennings, S. G., Berresheim, H., Wenger, J., Healy, R., Facchini, M. C., Rinaldi, M., Giulianelli, L., Finessi, E., Worsnop, D., Ehn, M., Mikkilä, J., Kulmala, M., and O'Dowd, C. D.: Aerosol properties associated with air masses arriving into the North East Atlantic during the 2008 Mace Head EUCAARI intensive observing period: an overview, Atmos. Chem. Phys., 10, 8413–8435, https://doi.org/10.5194/acp-10-8413-2010, 2010.

Dall'Osto, M., Monahan, C., Greaney, R., Beddows, D. C. S., Harrison, R. M., Ceburnis, D., and O'Dowd, C. D.: A statistical analysis of North East Atlantic (submicron) aerosol size distributions, Atmos. Chem. Phys., 11, 12567–12578, https://doi.org/10.5194/acp-11-12567-2011, 2011.

DeCarlo, P. F., Slowik, J. G., Worsnop, D. R., Davidovits, P., and Jimenez, J. L.: Particle Morphology and Density Characterization by Combined Mobility and Aerodynamic Diameter Measurements. Part 1: Theory, Aerosol Sci. Tech., 38, 1185–1205, https://doi.org/10.1080/027868290903907, 2004.

Deshmukh, S., Ferrer-Cid, P., Romshoo, B.,Poulain, L., Barcelo-Ordinas, J.M., Garcia-Vidal, J., Christodoulou, A., Bezantakos, S., Denjean, C., D'Anna, B., Formenti, P., Mukherjee, S., Habib, G., Kumar, P., Huang, S., Wu, Z., Wehner, B., Henning, S., Viana, M., Petters, M.D., Ahlawat, A., and Pöhlker, M.: Regional aerosol hygroscopicity influences radiative forcing globally, Commun Earth Environ., 7, 416, https://doi.org/10.1038/s43247-026-03505-z, 2026.

Dione, C., Haeffelin, M., Burnet, F., Lac, C., Canut, G., Delanoë, J., Dupont, J.-C., Jorquera, S., Martinet, P., Ribaud, J.-F., and Toledo, F.: Role of thermodynamic and turbulence processes on the fog life cycle during SOFOG3D experiment, Atmos. Chem. Phys., 23, 15711–15731, https://doi.org/10.5194/acp-23-15711-2023, 2023.

Dorman, C. E., Mejia, J., Koračin, D., and McEvoy, D.: World marine fog analysis based on 58-years of ship observations, Int. J. Climatol., 40, 145–168, https://doi.org/10.1002/joc.6200, 2020.

Doulgeris, K.-M., Komppula, M., Romakkaniemi, S., Hyvärinen, A.-P., Kerminen, V.-M., and Brus, D.: In situ cloud ground-based measurements in the Finnish sub-Arctic: intercomparison of three cloud spectrometer setups, Atmos. Meas. Tech., 13, 5129–5147, https://doi.org/10.5194/amt-13-5129-2020, 2020.

Dournaux, M., Tulet, P., Pianezze, J., Brioude, J., Metzger, J.-M., Thyssen, M., and Athier, G.: Origin, size distribution, and hygroscopic properties of marine aerosols in the southwestern Indian Ocean: results of six campaigns of shipborne observations, Atmos. Chem. Phys., 25, 10315–10335, https://doi.org/10.5194/acp-25-10315-2025, 2025.

Duplessis, P., Bhatia, S., Hartery, S., Wheeler, M. J., and Chang, R. Y. W.: Microphysics of aerosol, fog and droplet residuals on the Canadian Atlantic coast, Atmos. Res., 264, 105859, https://doi.org/10.1016/j.atmosres.2021.105859, 2021.

https://doi.org/10.5194/egusphere-2026-6260
Preprint. Discussion started: 19 November 2026
© Author(s) 2026. CC BY 4.0 License.

Dusek, U., Frank, G. P., Hildebrandt, L., Curtius, J., Schneider, J., Walter, S., Chand, D., Drewnick, F., Hings, S., Jung, D., Borrmann, S., and Andreae, M. O.: Size matters more than chem istry for cloud-nucleating ability of aerosol particles, Science, 312, 1375–1378, https://doi.org/10.1126/science.1125261, 2006.

Dye, J. E. and Baumgardner, D.: Evaluation of the forward scattering spectrometer probe, I – Electronic and optical studies, J. Atmos. Ocean. Technol., 1, 329–344, https://doi.org/10.1175/1520-0426(1984)001<0329:EOTFSS>2.0.CO;2, 1984.

Eger, P., Mathes, T., Zavarsky, A., and Duester, L.: Measurement report: Inland ship emissions and their contribution to NO_x and ultrafine particle concentrations at the Rhine, Atmos. Chem. Phys., 23, 8769–8788, https://doi.org/10.5194/acp-23-8769-2023, 2023.

Engelbrecht, F. A., Steinkopf, J., Padavatan, J., and Midgley, G. F.: Projections of Future Climate Change in Southern Africa and the Potential for Regional Tipping Points, in: Sustainability of Southern African Ecosystems under Global Change. Ecological Studies, edited by: von Maltitz, G. P., Midgley, G. F., Veitch, J., Brümmer, C., Rötter, R. P., Viehberg, F. A., and Veste, M., vol. 248, Springer, Cham, 169–190, https://doi.org/10.1007/978-3-031-10948-5_7, 2024.

Ervens, B., Sorooshian, A., Aldhaif, A. M., Shingler, T., Crosbie, E., Ziemba, L., Campuzano-Jost, P., Jimenez, J. L., and Wisthaler, A.: Is there an aerosol signature of chemical cloud processing?, Atmos. Chem. Phys., 18, 16099–16119, https://doi.org/10.5194/acp-18-16099-2018, 2018.

Fernando, H. J., Gultepe, I., Dorman, C., Pardyjak, E., Wang, Q., Hoch, S. W., Richter, D., Creegan, E., Gaberšek, S., Bullock, T., Hocut, C., Chang, R., Alappattu, D., Dimitrova, R., Flagg, D., Grachev, A., Krishnamurthy, R., Singh, D. K., Lozovatsky, I., Nagare, B., Sharma, A., Wagh, S., Wainwright, C., M. Wroblewski, M., Yamaguchi, R., Bardoel, S., Coppersmith, R. S., Chisholm, N., Gonzalez, E., Gunawardena, N., Hyde, O., Morrison, T., Olson, A., Perelet, A., Perrie, W., Wang, S., and Wauer, B.: C-FOG: life of coastal fog, B. Am. Meteorol. Soc., 102, E244–E272, https://doi.org/10.1175/BAMS-D-19-0070.1, 2021.

Formenti, P., Piketh, S. J., Namwoonde, A., Klopper, D., Burger, R., Cazaunau, M., Feron, A., Gaimoz, C., Broccardo, S., Walton, N., Desboeufs, K., Siour, G., Hanghome, M., Mafwila, S., Omoregie, E., Junkermann, W., and Maenhaut, W.: Three years of measurements of light-absorbing aerosols over coastal Namibia: seasonality, origin, and transport, Atmos. Chem. Phys., 18, 17003–17016, https://doi.org/10.5194/acp-18-17003-2018, 2018.

Formenti, P., D'Anna, B., Flamant, C., Mallet, M., Piketh, S. J., Schepanski, K., Waquet, F., Auriol, F., Brogniez, G., Burnet, F., Chaboureau, J., Chauvigné, A., Chazette, P., Denjean, C., Desboeufs, K., Doussin, J., Elguindi, N., Feuerstein, S., Gaetani, M., Giorio, C., Klopper, D., Mallet, M. D., Nabat, P., Monod, A., Solmon, F., Namwoonde, A., Chikwililwa, C., Mushi, R., Welton, E. J., and Holben, B.: The Aerosols, Radiation and Clouds in Southern Africa Field Campaign in Namibia: Overview, illustrative observations, and way forward, B. Am. Meteor. Soc., 100, 1277–1298, https://doi.org/10.1175/BAMS-D-17-0278.1, 2019.

Formenti, P., Giorio, C., Desboeufs, K., Zherebker, A., Gaetani, M., Baldo, C., Landrot, G., Montebello, S., Chevaillier, S., Triquet, S., Siour, G., Di Biagio, C., Battaglia, F., Doussin, J.-F., Feron, A., Namwoonde, A., and Piketh, S. J.: Elemental composition, iron mineralogy, and solubility of anthropogenic and natural mineral dust aerosols in Namibia: a case study

© Author(s) 2026. CC BY 4.0 License.

analysis from the AEROCLO-sA campaign – Part 2, Atmos. Chem. Phys., 25, 16127–16145, https://doi.org/10.5194/acp-25-16127-2025, 2025.

Formenti, P., Klopper, D., Feron, A., Cazaunau, M., Chevaillier, S., Desboeufs, K., Di Biagio, C., Baldo, C., Gaimoz, C., Michoud, V., Mirande-Bret, C., Triquet, S., Hemeret, F., Valorso, R., Broccardo, S., Namwoonde, A., Hanghome, M., Giorio, C., and Piketh, S. J.: Dataset of aerosol, ozone, and meteorology observations at the surface coastal site of Henties Bay in Namibia, Earth Syst. Sci. Data Discuss. [preprint], https://doi.org/10.5194/essd-2026-95, in review, 2026.

Ghosh, P., Boutle, I., Field, P., Hill, A., Jones, A., Mazoyer, M., Evans, K. J., Mahajan, S., Kang, H.-G., Xu, M., Zhang, W., Asch, N., and Gordon, H.: High sensitivity of simulated fog properties to parameterized aerosol activation in case studies from ParisFog, Atmos. Chem. Phys., 25, 11129–11156, https://doi.org/10.5194/acp-25-11129-2025, 2025.

Giorio, C., Doussin, J. F., D'Anna, B., Mas, S., Filippi, D., Denjean, C., Mallet, M. D., Bourrianne, T., Burnet, F, Cazanaur, M., Chikwililwa, C., Desboeufs, K., Feron, A., Michoud, V., Namwoonde, A., Andreae, M. O., Piketh, S. J., and Formenti, P.: Butene emissions from coastal ecosystems may contribute to new particle formation, Geophys. Res. Lett., 49, e2022GL098770, https://doi.org/10.1029/2022GL098770, 2022.

Gong, X., Wang, Y., Xie, H., Zhang, J., Lu, Z., Wood, R., Stratmann, F., Wex, H., Liu, X., and Wang, J.: Maximum Supersaturation in the Marine Boundary Layer Clouds Over the North Atlantic, AGU Advances, 4, e2022AV000855, https://doi.org/10.1029/2022AV000855, 2023.

Gysel, M., Crosier, J., Topping, D. O., Whitehead, J. D., Bower, K. N., Cubison, M. J., Williams, P. I., Flynn, M. J., McFiggans, G. B., and Coe, H.: Closure study between chemical composition and hygroscopic growth of aerosol particles during TORCH2, Atmos. Chem. Phys., 7, 6131–6144, https://doi.org/10.5194/acp-7-6131-2007, 2007.

Heim, M., Mullins, B. J., Umhauer, H., and Kasper, G.: Performance evaluation of three optical particle counters with an efficient "multimodal" calibration method, J. Aerosol Sci., 39, 1019–1031, https://doi.org/10.1016/j.jaerosci.2008.07.006, 2008.

Henning, S., Dieckmann, K., Ignatius, K., Schäfer, M., Zedler, P., Harris, E., Sinha, B., van Pinxteren, D., Mertes, S., Birmili, W., Merkel, M., Wu, Z., Wiedensohler, A., Wex, H., Herrmann, H., and Stratmann, F.: Influence of cloud processing on CCN activation behaviour in the Thuringian Forest, Germany during HCCT-2010, Atmos. Chem. Phys., 14, 7859–7868, https://doi.org/10.5194/acp-14-7859-2014, 2014.

Hersbach, H., Bell, B., Berrisford, P., Hirahara, S., Horányi, A., Muñoz-Sabater, J., Nicolas, J., Peubey, C., Radu, R., Schepers, D., Simmons, A., Soci, C., Abdalla, S., Abellan, X., Balsamo, G., Bechtold, P., Biavati, G., Bidlot, J., Bonavita, M., De Chiara, G., Dahlgren, P., Dee, D., Diamantakis, M., Dragani, R., Flemming, J., Forbes, R., Fuentes, M., Geer, A., Haimberger, L., Healy, S., Hogan, R. J., Hólm, E., Janisková, M., Keeley, S., Laloyaux, P., Lopez, P., Lupu, C., Radnoti, G., de Rosnay, P., Rozum, I., Vamborg, F., Villaume, S., and Thépaut, J.-N.: The ERA5 global reanalysis, Q. J. Roy. Meteor. Soc., 146, 1999–2049, https://doi.org/10.1002/qj.3803, 2020.

Hilario, M. R. A., Crosbie, E., Shook, M., Reid, J. S., Cambaliza, M. O. L., Simpas, J. B. B., Ziemba, L., DiGangi, J. P., Diskin, G. S., Nguyen, P., Turk, F. J., Winstead, E., Robinson, C. E., Wang, J., Zhang, J., Wang, Y., Yoon, S., Flynn, J., Alvarez, S.

https://doi.org/10.5194/egusphere-2026-6260
Preprint. Discussion started: 19 November 2026
© Author(s) 2026. CC BY 4.0 License.

L., Behrangi, A., and Sorooshian, A.: Measurement report: Long-range transport patterns into the tropical northwest Pacific during the CAMP^{2}Ex aircraft campaign: chemical composition, size distributions, and the impact of convection, Atmos. Chem. Phys., 21, 3777–3802, https://doi.org/10.5194/acp-21-3777-2021, 2021.

Hipler, V., Andersen, H., Spirig, R., Vogt, R., Piketh, S., Adler, B., and Cermak, J.: Synoptic and regional-scale meteorological controls of stratus altitude in the Namib Desert, EGUsphere [preprint], https://doi.org/10.5194/egusphere-2025-5816, 2026.

Huang, S., Wu, Z., Poulain, L., van Pinxteren, M., Merkel, M., Assmann, D., Herrmann, H., and Wiedensohler, A.: Source apportionment of the organic aerosol over the Atlantic Ocean from 53° N to 53° S: significant contributions from marine emissions and long-range transport, Atmos. Chem. Phys., 18, 18043–18062, https://doi.org/10.5194/acp-18-18043-2018, 2018.

Isaac, G. A., Bullock, T., Beale, J., and Beale, S.: Characterizing and Predicting Marine Fog Offshore Newfoundland and Labrador, Weather Forecast., 35, 347–365, https://doi.org/10.1175/WAF-D-19-0085.1, 2020.

Jones, A., Thomson, D., Hort, M., and Devenish, B.: The UK Met Office's next-generation atmospheric dispersion model, NAME III, Air Pollut. Model. Appl. XVII, 17, 580–589, https://doi.org/10.1007/978-0-387-68854-1_62, 2007.

Kaseke, K. F., Wang, L., and Seely, M. K.: Non rainfall water origins and formation mechanisms, Sci. Adv., 3, e1603131, https://doi.org/10.1126/sciadv.1603131, 2017.

Kaseke, K. F., Tian, C., Wang, L., Seely, M., Vogt, R., Wassenaar, T., and Mushi, R.: Fog spatial distributions over the Central Namib Desert-an isotope approach, Aerosol and Air Quality Research, 18, 49–61, https://doi.org/10.4209/aaqr.2017.01.0062, 2018.

Kaspar, F., Helmschrot, J., Mhanda, A., Butale, M., de Clercq, W., Kanyanga, J. K., Neto, F. O. S., Kruger, S., Castro Matsheka, M., Muche, G., Hillmann, T., Josenhans, K., Posada, R., Riede, J., Seely, M., Ribeiro, C., Kenabatho, P., Vogt, R., and Jürgens, N.: The SASSCAL contribution to climate observation, climate data management and data rescue in Southern Africa, Adv. Sci. Res., 12, 171–177, https://doi.org/10.5194/asr-12-171-2015, 2015.

Kawana, K., Miyazaki, Y., Omori, Y., Tanimoto, H., Kagami, S., Suzuki, K., Yamashita, Y., Nishioka, J., Deng, Y., Yai, H., and Mochida, M.: Number-Size Distribution and CCN Activity of Atmospheric Aerosols in the Western North Pacific During Spring Pre-Bloom Period: Influences of Terrestrial and Marine Sources, J. Geophys. Res.-Atmos., 127, e2022JD036690, https://doi.org/10.1029/2022JD036690, 2022.

Klopper, D., Formenti, P., Namwoonde, A., Cazaunau, M., Chevaillier, S., Feron, A., Gaimoz, C., Hease, P., Lahmidi, F., Mirande-Bret, C., Triquet, S., Zeng, Z., and Piketh, S. J.: Chemical composition and source apportionment of atmospheric aerosols on the Namibian coast, Atmos. Chem. Phys., 20, 15811–15833, https://doi.org/10.5194/acp-20-15811-2020, 2020.

Leipper, D. F.: Fog on the US west coast: A review, B. Am. Meteorol. Soc., 75, 229–240, https://doi.org/10.1175/1520-0477(1994)075<0229:FOTUWC>2.0.CO;2,1994.

Li, Y., Marais, E., and Wang, L.: Decade-long isotope dataset of rainfall and non-rainfall waters in the central Namib Desert, Earth Syst. Sci. Data Discuss. [preprint], https://doi.org/10.5194/essd-2026-170, in review, 2026.

Liu, Q., Wu, B., Wang, Z., and Hao, T.: Fog Droplet Size Distribution and the Interaction between Fog Droplets and Fine Particles during Dense Fog in Tianjin, China, Atmosphere, 11, 258 pp., https://doi.org/10.3390/atmos11030258, 2020.

https://doi.org/10.5194/egusphere-2026-6260
Preprint. Discussion started: 19 November 2026
© Author(s) 2026. CC BY 4.0 License.

Liu, Q., Shen, X., Sun, J., Zhang, Y., Qi, B., Ma, Q., Han, L., Xu, H., Hu, X., Lu, J., Liu, S., Yu, A., Liang, L., Gao, Q., Wang, H., Che, H., and Zhang, X.: Characterization of fog microphysics and their relationships with visibility at a mountain site in China, Atmos. Chem. Phys., 25, 3253–3267, https://doi.org/10.5194/acp-25-3253-2025, 2025.

Malik, D., Andersen, H., Cermak, J., Vogt, R., and Adler, B.: Cloud base height determines fog occurrence patterns in the Namib Desert, Atmos. Chem. Phys., 26, 681–701, https://doi.org/10.5194/acp-26-681-2026, 2026.

Mandariya, A. K., Ahlawat, A., Haneef, M., Baig, N. A., Patel, K., Apte, J., Hildebrandt Ruiz, L., Wiedensohler, A., and Habib, G.: Measurement report: Hygroscopicity of size-selected aerosol particles in the heavily polluted urban atmosphere of Delhi: impacts of chloride aerosol, Atmos. Chem. Phys., 24, 3627–3647, https://doi.org/10.5194/acp-24-3627-2024, 2024.

Mazoyer, M., Burnet, F., Denjean, C., Roberts, G. C., Haeffelin, M., Dupont, J.-C., and Elias, T.: Experimental study of the aerosol impact on fog microphysics, Atmos. Chem. Phys., 19, 4323–4344, https://doi.org/10.5194/acp-19-4323-2019, 2019.

Mazoyer, M., Burnet, F., and Denjean, C.: Experimental study on the evolution of droplet size distribution during the fog life cycle, Atmos. Chem. Phys., 22, 11305–11321, https://doi.org/10.5194/acp-22-11305-2022, 2022.

Meng, J. W., Yeung, M. C., Li, Y. J., Lee, B. Y. L., and Chan, C. K.: Size-resolved cloud condensation nuclei (CCN) activity and closure analysis at the HKUST Supersite in Hong Kong, Atmos. Chem. Phys., 14, 10267–10282, https://doi.org/10.5194/acp-14-10267-2014, 2014.

Mitchell, D., J. R. Henschel, R. S. Hetem, T. D. Wassenaar, W. M. Strauss, S. A. Hanrahan, and M. K. Seely.: Fog and fauna of the Namib Desert: past and future, Ecosphere, 11, 1, e02996, https://doi.org/10.1002/ecs2.2996, 2020.

Nault, B. A., Canagaratna, M., Croteau, P., Fortner, E., Lambe, A. T., Stark, H., Sueper, D., Werden, B. S., Williams, A., Williams, L. R., Worsnop, D., Jayne, J., DeCarlo, P. F., Cubison, M., Papadopoulos, G., and Urs, R.: Characterization of a new higher-resolution time-of-flight aerosol chemical speciation monitor: Application for measurements of atmospheric aerosols, Aerosol Sci. Tech., 59, 719–742, https://doi.org/10.1080/02786826.2025.2481221, 2025.

Ndarana, T., Bopape, M.-J., Waugh, D., and Dyson, L.: The influence of the lower stratosphere on ridging Atlantic Ocean anticyclones over South Africa, Journal of Climate, 31, 6175–6187, https://doi.org/10.1175/JCLI-D-17-0832.1, 2018.

Nelli, N., Francis, D., Abida, R., Fonseca, R., Masson, O., and Bosc, E.: In-situ measurements of fog microphysics: Visibility parameterization and estimation of fog droplet sedimentation velocity, Atmos. Res., 309, 107570, https://doi.org/10.1016/j.atmosres.2024.107570, 2024.

Olivier, J. and Stockton, P.: The influence of upwelling extent upon fog incidence at Lüderitz, southern Africa, International Journal of Climatology, 9, 69–75, https://doi.org/10.1002/joc.3370090106, 1989.

Ovadnevaite, J., Ceburnis, D., Canagaratna, M., Berresheim, H., Bialek, J., Martucci, G., Worsnop, D. R., and O'Dowd, C.: On the effect of wind speed on submicron sea salt mass concentrations and source fluxes, J. Geophys. Res.-Atmos., 117, D16201, https://doi.org/10.1029/2011JD017379, 2012.

Petters, M. D. and Kreidenweis, S. M.: A single parameter representation of hygroscopic growth and cloud condensation nucleus activity, Atmos. Chem. Phys., 7, 1961–1971, https://doi.org/10.5194/acp-7-1961-2007, 2007.

https://doi.org/10.5194/egusphere-2026-6260
Preprint. Discussion started: 19 November 2026
© Author(s) 2026. CC BY 4.0 License.

Pinsky, M., and Khain, A.: Calculation of Supersaturation Maximum and Droplet Concentration at Cloud Boundaries, *Atmos. Res.,* 234, 104694, https://doi.org/10.1016/j.atmosres.2019.104694, 2020.

Pöhlker, M. L., Pöhlker, C., Ditas, F., Klimach, T., Hrabe de Angelis, I., Araújo, A., Brito, J., Carbone, S., Cheng, Y., Chi, X., Ditz, R., Gunthe, S. S., Kesselmeier, J., Könemann, T., Lavrič, J. V., Martin, S. T., Mikhailov, E., Moran-Zuloaga, D., Rose, D., Saturno, J., Su, H., Thalman, R., Walter, D., Wang, J., Wolff, S., Barbosa, H. M. J., Artaxo, P., Andreae, M. O., and Pöschl, U.: Long-term observations of cloud condensation nuclei in the Amazon rain forest – Part 1: Aerosol size distribution, hygroscopicity, and new model parametrizations for CCN prediction, Atmos. Chem. Phys., 16, 15709–15740, https://doi.org/10.5194/acp-16-15709-2016, 2016.

Poku, C., Ross, A. N., Hill, A. A., Blyth, A. M., and Shipway, B.: Is a more physical representation of aerosol activation needed for simulations of fog?, Atmos. Chem. Phys., 21, 7271–7292, https://doi.org/10.5194/acp-21-7271-2021, 2021.

Pope, N. H. and Igel, A. L.: Counteracting influences of gravitational settling modulate aerosol impacts on cloud-base-lowering fog characteristics, Atmos. Chem. Phys., 25, 5433–5444, https://doi.org/10.5194/acp-25-5433-2025, 2025.

Rinaldi, M., Facchini, M. C., Decesari, S., Carbone, C., Finessi, E., Mircea, M., Fuzzi, S., Ceburnis, D., Ehn, M., Kulmala, M., de Leeuw, G., and O'Dowd, C. D.: On the representativeness of coastal aerosol studies to open ocean studies: Mace Head – a case study, Atmos. Chem. Phys., 9, 9635–9646, https://doi.org/10.5194/acp-9-9635-2009, 2009.

Rinaldi, M., Fuzzi, S., Decesari, S., Marullo, S., Santoleri, R., Provenzale, A., von Hardenberg, J., Ceburnis, D., Vaishya, A., O'Dowd, C. D., and Facchini, M. C.: Is chlorophyll *a* the best surrogate for organic matter enrichment in submicron primary marine aerosol?, J. Geophys. Res.-Atmos., 118, 4964–4973, https://doi.org/10.1002/jgrd.50417, 2013.

Rogers, R. R. and Yau, M. K.: A Short Course in Cloud Physics, 3rd Edn., in: International Series in Natural Philosophy, Vol. 113, Pergamon Press, 1989.

Rohde, R. F., Hoffman, M. T., Durbach, I., Venter, Z., and Jack, S.: Vegetation and climate change in the Pro-Namib and Namib Desert based on repeat photography: Insights into climate trends, Journal of Arid Environments, 165, 119–131, https://doi.org/10.1016/j.jaridenv.2019.01.007, 2019.

Román-Cascón, C., Yagüe, C., Steeneveld, G.-J., Morales, G., Arrillaga, J. A., Sastre, M., and Maqueda, G.: Radiation and cloud-base lowering fog events: Observational analysis and evaluation of WRF and HARMONIE, Atmos. Res., 229, 190–207, https://doi.org/10.1016/j.atmosres.2019.06.018, 2019.

Royer, H. M., Pöhlker, M. L., Krüger, O., Blades, E., Sealy, P., Lata, N. N., Cheng, Z., China, S., Ault, A. P., Quinn, P. K., Zuidema, P., Pöhlker, C., Pöschl, U., Andreae, M., and Gaston, C. J.: African smoke particles act as cloud condensation nuclei in the wintertime tropical North Atlantic boundary layer over Barbados, Atmos. Chem. Phys., 23, 981–998, https://doi.org/10.5194/acp-23-981-2023, 2023.

Schmale, J., Schneider, J., Nemitz, E., Tang, Y. S., Dragosits, U., Blackall, T. D., Trathan, P. N., Phillips, G. J., Sutton, M., and Braban, C. F.: Sub-Antarctic marine aerosol: dominant contributions from biogenic sources, Atmos. Chem. Phys., 13, 8669–8694, https://doi.org/10.5194/acp-13-8669-2013, 2013.

https://doi.org/10.5194/egusphere-2026-6260
Preprint. Discussion started: 19 November 2026
© Author(s) 2026. CC BY 4.0 License.

Seely, M. K. and Henschel, J. R.: The climatology of Namib fog, in: Proceedings of the First International Conference on Fog and Fog Collection, pp. 353–356, 1998.

Seppälä, S. D., Kuula, J., Hyvärinen, A.-P., Saarikoski, S., Rönkkö, T., Keskinen, J., Jalkanen, J.-P., and Timonen, H.: Effects of marine fuel sulfur restrictions on particle number concentrations and size distributions in ship plumes in the Baltic Sea, Atmos. Chem. Phys., 21, 3215–3234, https://doi.org/10.5194/acp-21-3215-2021, 2021.

Shanyengana, E. S., Henschel, J. R., Seely, M. K., and Sanderson, R. D.: Exploring fog as a supplementary water source in Namibia, Atmos. Res., 64, 251–259, https://doi.org/10.1016/S0169-8095(02)00096-0, 2002.

Shen, C., Zhao, C., Ma, N., Tao, J., Zhao, G., Yu, Y., and Kuang, Y.: Method to Estimate Water Vapor Supersaturation in the Ambient Activation Process Using Aerosol and Droplet Measurement Data, J. Geophys. Res.-Atmos., 123, 10606–10619, https://doi.org/10.1029/2018JD028315, 2018.

Spirig, R., Vogt, R., Larsen, J. A., Feigenwinter, C., Wicki, A., Franceschi, J., Parlow, E., Adler, B., Kalthoff, N., Cermak, J., Andersen, H., Fuchs, J., Bott, A., Hacker, M., Wagner, N., Maggs-Kölling, G., Wassenaar, T., and Seely, M.: Probing the fog life cycles in the Namib Desert, B. Am. Meteor. Soc., 100, 2491–2507, https://doi.org/10.1175/BAMS-D-18-0142.1, 2019.

Tlhalerwa, K., Freiman, M. T., and Piketh, S. J.: Aerosol Deposition off the Southern African West Coast by Berg Winds, S. Afr. Geogr. J., 87, 152–161, https://doi.org/10.1080/03736245.2005.9713838, 2012.

Tsai, I.-C., Hsieh, P.-R., Cheung, H. C., and Chung-Kuang Chou, C.: Aerosol impacts on fog microphysics over the western side of Taiwan Strait in April from 2015 to 2017, Atmos. Environ., 262, 118523, https://doi.org/10.1016/j.atmosenv.2021.118523, 2021.

Ueda, S., Miura, K., Kawata, R., Furutani, H., Uematsu, M., Omori, Y., and Tanimoto, H.: Number–size distribution of aerosol particles and new particle formation events in tropical and subtropical Pacific Oceans, Atmos. Environ., 142, 324–339, https://doi.org/10.1016/j.atmosenv.2016.07.055, 2016.

Wainwright, C., Chang, R. Y.-W., and Richter, D.: Aerosol Activation in Radiation Fog at the Atmospheric Radiation Program Southern Great Plains Site, J. Geophys. Res.-Atmos., 126, e2021JD035358, https://doi.org/10.1029/2021JD035358, 2021.

Wang, Q., Yamaguchi, R. T., Kalogiros, J. A., Daniels, Z., Alappattu, D. P., Jonsson, H., Alvarenga, O., Olson, A., Wauer, B. J., Ortiz-Suslow, D. G., and Fernando, H. J.: Microphysics and Optical Attenuation in Fog: Observations from Two Coastal Sites, Bound.-Lay. Meteorol., 181, 267–292, https://doi.org/10.1007/s10546-021-00675-5, 2021.

Weathers, K. C., Ponette-González, A. G., and Dawson, T. E.: Medium, vector, and connector: Fog and the maintenance of ecosystems, Ecosystems, 23, 217–229, https://doi.org/10.1007/s10021-019-00388-4, 2020.

Weston, M. J., Piketh, S. J., Burnet, F., Broccardo, S., Denjean, C., Bourrianne, T., and Formenti, P.: Sensitivity analysis of an aerosol-aware microphysics scheme in Weather Research and Forecasting (WRF) during case studies of fog in Namibia, Atmos. Chem. Phys., 22, 10221–10245, https://doi.org/10.5194/acp-22-10221-2022, 2022.

Wex, H., McFiggans, G., Henning, S., and Stratmann, F.: Influence of the external mixing state of atmospheric aerosol on derived CCN number concentrations, Geophys. Res. Lett., 37, L10805, https://doi.org/10.1029/2010gl043337, 2010.

https://doi.org/10.5194/egusphere-2026-6260
Preprint. Discussion started: 19 November 2026
© Author(s) 2026. CC BY 4.0 License.

Wu, H., Peers, F., Taylor, J. W., Yu, C., Abel, S. J., Barrett, P. A., Trembath, J., Bower, K., Haywood, J. M., and Coe, H.: The transport history of African biomass burning aerosols arriving in the remote Southeast Atlantic and their impacts on cloud properties, Atmos. Chem. Phys., 25, 16589–16609, https://doi.org/10.5194/acp-25-16589-2025, 2025.

Xu, W., Ovadnevaite, J., Fossum, K. N., Lin, C., Huang, R.-J., O'Dowd, C., and Ceburnis, D.: Aerosol hygroscopicity and its link to chemical composition in the coastal atmosphere of Mace Head: marine and continental air masses, Atmos. Chem. Phys., 20, 3777–3791, https://doi.org/10.5194/acp-20-3777-2020, 2020.

Xu, W., Fossum, K. N., Ovadnevaite, J., Lin, C., Huang, R.-J., O'Dowd, C., and Ceburnis, D.: The impact of aerosol size-dependent hygroscopicity and mixing state on the cloud condensation nuclei potential over the north-east Atlantic, Atmos. Chem. Phys., 21, 8655–8675, https://doi.org/10.5194/acp-21-8655-2021, 2021.

Xu, W., Ovadnevaite, J., Fossum, K. N., Huang, R.-J., Huang, D. D., Zhong, H., Gu, Y., Lin, C., Huang, C., O'Dowd, C., and Ceburnis, D.: Condensation of organic-inorganic vapours governs the production of ultrafine secondary marine cloud nuclei, Communications Earth & Environment, 5, 359, https://doi.org/10.1038/s43247-024-01519-z, 2024.

Yan, S., Zhu, B., Zhu, T., Shi, C., and Liu, D.: The Effect of Aerosols on Fog Lifetime: Observational Evidence and Model Simulations, Geophys. Res. Lett., 48, e2020GL61803, https://doi.org/10.1029/2020GL091156, 2021.

Yu, C., Pasternak, D., Lee, J., Yang, M., Bell, T., Bower, K., Wu, H., Liu, D., Reed, C., Bauguitte, S., Cliff, S., Trembath, J., Coe, H., and Allan, J. D.: Characterizing the Particle Composition and Cloud Condensation Nuclei from Shipping Emission in Western Europe, Environ. Sci. Technol., 54, 15604–15612, https://doi.org/10.1021/acs.est.0c04039, 2020.